

Substorm Injection Modeling With Non-Dipolar, Time-Dependent Background Field

Sorin Zaharia, J. Birn, R. H. W. Friedel, G. D. Reeves and M. F. Thomsen

Los Alamos National Laboratory, Los Alamos, NM 87545

C. Z. Cheng

Princeton Plasma Physics Laboratory, Princeton University, Princeton, NJ 08543

Abstract. We model energetic particle injections during substorms by investigating the particle interaction with an Earthward-propagating electromagnetic pulse of spatially-localized transient electric and magnetic fields, superposed over a background magnetic field. The current work extends our previous model by considering the background field to be non-dipolar (stretched) before the arrival of the pulse (i.e. during the substorm growth phase), and changing in a time-dependent manner and becoming a dipole field in the wake of the pulse. The particle motion still conserves the first adiabatic invariant, even in the stretched magnetic field, and both protons and electrons are convected Earthward by the $\mathbf{E} \times \mathbf{B}$ drift to regions of higher field values, undergoing betatron acceleration. As in the previous model, we find fully-analytical solutions for the particle gyrocenter motion, and we apply these solutions to compute the injected particle flux. We discuss how the model can explain several substorm injection features such as the low/high energy cutoffs and finally we apply the model solutions to a simulation of an actual injection event, obtaining good agreement with observations. The current results with the more realistic background field show significant increase in particle flux enhancement for “substorm energies” (tens to hundreds of keVs) and typical pulse parameters compared to the case of a dipole background, leading to the conclusion that the particles have to arrive from closer to Earth than obtained before in order to explain the observed injected flux levels. The new model provides a better fit to observations than the previous study, because it requires lower transient electric fields (more realistic of a typical substorm), and thus better explains the ubiquity of particle injections associated with substorms.

1. Introduction

One of the most typical indicators of a magnetospheric substorm onset is the “injection” of high-energy particles (typically between tens and a few hundred keVs) into the nightside region of the magnetosphere. During a substorm injection, the particle energization can be almost simultaneous for a wide range of energies — the rise in particle flux for different energies occurs within 1 min. In such a case, the injection is called “dispersionless.” Dispersionless injections, characterized by sudden, large increases in particle fluxes (one to two orders of magnitude), are generally localized near midnight in local time [Belian *et al.*, 1978; Lopez *et al.*, 1990; Thomsen *et al.*, 2001] (with the exception of a few which can occur away from midnight [Friedel *et al.*, 1996]), and are confined to a rather narrow local-time “wedge” of typically 60° to 70° [e.g., Clauer and McPherron, 1974].

Another interesting property of the injections is that there seems to be a clear radial propagation pattern in the Earthward direction: radially displaced satellites have definitely shown [Russell and McPherron, 1973; Moore *et al.*, 1981; Reeves *et al.*, 1996] that the injection occurs first at the outer satellite.

In order to explain where the injected particles come from and what their energization mechanism is, injections of particles with “substorm energies” (up to a few hundred

keV) have been successfully modeled by tracing the particle motion in given electric and magnetic fields [Birn *et al.*, 1997b, 1998; Li *et al.*, 1998; Zaharia *et al.*, 2000; Birn *et al.*, 2003]. While Birn *et al.* compute the motion in the time-dependent fields of an MHD simulation, the models of Li *et al.* [1998] and Zaharia *et al.* [2000] postulate an electromagnetic “dipolarization pulse” originating at the time of substorm onset and propagating Earthward, and analyze individual particle motion in the combined fields of the pulse and a dipolar background magnetic field. In such a model the particles are transported adiabatically Earthward by the $\mathbf{E} \times \mathbf{B}$ drift and accelerated via betatron acceleration. The work of Li *et al.* [1998] (and its later refinement by Sarris *et al.* [2002]) presents numerical solutions for the particle trajectories, while Zaharia *et al.* [2000] manage to find analytical solutions for the particle motion, with both studies showing good agreement between predicted fluxes and observations. The results of Li *et al.* and Zaharia *et al.* do differ in an important aspect, however, and that is the source location for the particles that arrive at geostationary orbit. While Li *et al.* obtain from their electron injection analysis that more than 90% of the enhancement is due to electrons originally at $R_0 > 9 R_E$, Zaharia *et al.* find that virtually all particles arrive from distances less than $9 R_E$ from Earth.

While these types of particle tracing models do not try to explain how the dipolarization pulse forms, there is ample observational verification at the time of substorm onset of such electromagnetic pulses, characterized by transient electric and magnetic fields. For example, Sheperd *et al.* [1980] found from Geos 2 observations that large transient westward electric fields exist in the plasma sheet during the

substorm expansion phase. These fields can have very large magnitudes, with documented values as high as 50 mV/m [Fairfield *et al.*, 1998]. In an electromagnetic pulse, the electric field is accompanied by an inductively-consistent magnetic field. Such a field has been observed as well, and studies [Aggson *et al.*, 1983] have demonstrated a clear correlation between the electric and magnetic field fluctuations, i.e. their inductive nature.

The present work is an extension of our previous study [Zaharia *et al.*, 2000] of particle injections. We pursue two objectives in this paper. The main goal consists in improving the transport model for the injected particles. While the previous pulse models [Li *et al.*, 1998; Zaharia *et al.*, 2000] strive to assign realistic, observation-based parameters for the dipolarization pulse, they use dipolar configurations to represent the background magnetic field over which the pulse field is superposed. Even though the models modify the dipole field values to take into the account the diamagnetic effect of the ring current, this is insufficient in the magnetotail, where the cross-tail current has a strong effect and dramatically changes the dipolar configuration, especially during times such as the substorm growth phase. Due to the large discrepancy between a dipolar field and the real field configuration (and their different variation with distance from Earth), the dipole choice is a simplification which can adversely affect the model results.

It is well known that during the growth phase the magnetic field lines become quite stretched (“tail-like”) in the near-Earth magnetotail, even at geosynchronous orbit [e.g., Kaufmann, 1987; Maynard *et al.*, 1996], with field values significantly decreased compared to quiet times (and to a dipolar configuration). The discrepancy between the real and the dipolar configuration during the growth phase is even more accentuated farther in the magnetotail. For example, in the equatorial plane at 15 R_E the dipole model would result in a value of 9 nT for the magnetic field, whereas the actual field value during disturbed conditions is much lower: for example the T96 empirical model [Tsyganenko, 1995; Tsyganenko and Stern, 1996] with parameters $B_{ZIMF} = -5$ nT, $B_{YIMF} = 0$, $P_{SW} = 3.5$ nT and $D_{st} = -5$ rnmT predicts a value of only about 2 nT there. To address this issue, the new background magnetic field used in this study is significantly stretched (i.e. field values much lower in the equatorial plane) compared to a dipole field before the dipolarization (substorm onset) and only returns to a dipolar configuration after the dipolarization wave has passed.

A second, less central objective of the present work is a more detailed discussion of the physical features of our model, and how the particle injection process depends on the different model parameters. While in our previous study [Zaharia *et al.*, 2000] we presented computations of particle fluxes for different injections, in this paper we will also investigate how observational constraints in conjunction with model results can impose physical limits on the model parameters, and also how the model can explain other features of the injection process, such as the observed “cutoffs” in injected fluxes during substorms, seen at both low and high energies.

As in our previous study, we obtain analytical solutions for the particle orbits, greatly reducing the amount of computational work needed for the flux calculation. The availability of analytical solutions combined with the relatively small number of parameters in the model provide increased physical insight into the transport and acceleration mechanisms and their dependence on physical quantities describing the dipolarization process.

The main result of the present work is that with a more realistic background magnetic field taken into account, the particle flux increase is significantly larger than in the case of dipolar background, for the same pulse parameters. This fact arises as a combined consequence of two opposing but

unequal effects: the slightly lower transport is more than counteracted by a higher effectiveness of betatron acceleration with the more realistic background field. The latter is due to the fact that the ratio between the final field and the field at the particle’s initial position is larger in this model than in the case of a dipolar background (for the same two locations). The larger energization leads to another conclusion, that particles injected at geosynchronous orbit arrive from even closer distances in the near-Earth plasma sheet (1 or 2 R_E away from geosynchronous) and that even modest substorm electric fields are sufficient for explaining the observed flux increases. The new model, by requiring lower transient electric fields (more realistic of a typical substorm than the ones in the previous study) provides a better fit to observations of substorm injections and better explains the ubiquity of the injections as one of the most reliable predictors of substorm onset.

The organization of the paper is as follows: In Section 2 we lay out the theoretical details of the particle transport and energization in the fields of a prescribed dipolarization pulse superposed on a time-dependent background field, which allows for completely analytical solutions for the particle gyrocenter (the solutions proper are presented in the Appendix). Section 3 presents and discusses the obtained particle trajectories with realistic parameters as input. We also discuss the low and high-energy injection cutoffs, compare the energization with the previous case and present constraints imposed by the results on the model parameters. Once the particle orbits are found, the fluxes can be easily computed using Liouville’s theorem. The flux computation at “virtual” satellites and comparison with previous computations and with geosynchronous satellite observations are presented in Section 4. Section 5 further discusses the model results, summarizes the paper and presents several conclusions.

2. Model

As in our previous study [Zaharia *et al.*, 2000], we assume that at substorm onset an Earthward-propagating dipolarization wave is generated, i.e. an electromagnetic pulse with velocity \mathbf{V}_0 , westward \mathbf{E} and consistent (inductive) $\delta\mathbf{B}$ fields. This pulse will be superposed on a new, more realistic background field, which will change from a stretched structure before the pulse (i.e. during the growth phase) to a dipolar one in the wake of the pulse. Before discussing the background field, let us analyze the pulse proper. The electric (E_ϕ) and magnetic (δB_Z) fields of the pulse are linked through Faraday’s law, whose component in the Z -direction

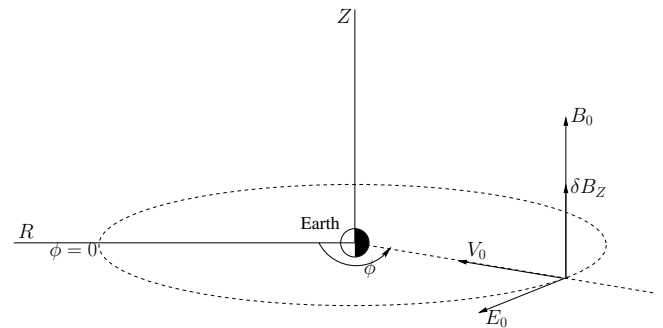


Figure 1. Electric and magnetic fields in the midnight sector in the cylindrical coordinate system (R, ϕ, Z) centered at Earth. The westward E_ϕ and northward δB_Z are the transient fields of the Earthward-propagating pulse; B_0 represents the background magnetic field (cf. [Zaharia *et al.*, 2000]).

of a cylindrical coordinate system (Equation 2 of [Zaharia *et al.*, 2000]) is (assuming for now that the background field is time-independent)

$$\frac{\partial}{\partial R}(RE_\phi) = -\frac{\partial(R\delta B_Z)}{\partial t} \quad (1)$$

The cylindrical coordinate system (R, ϕ, Z) has $R = 0$ at the center of the Earth, $Z = 0$ defining the equatorial plane (in this paper by “equator” we mean “magnetic equator”), and ϕ zero at noon local time and positive towards dusk (see Figure 1). This choice for ϕ is slightly different from the one in the previous work, and has been chosen to allow a better connection with the commonly-used GSM magnetospheric coordinate system. Solving as before Equation (1) one obtains for a pulse propagating Earthward (i.e. towards lower R) with a constant velocity V_0 the general solutions (starting from zero perturbation fields, and with time-independent background field) in the form [Zaharia *et al.*, 2000]

$$RE_\phi = f(R + V_0t, \phi) \quad (2)$$

$$R\delta B_Z = -\frac{f(R + V_0t, \phi)}{V_0} \quad (3)$$

As the electric field is westward ($E_\phi < 0$) and $V_0 > 0$, one has $\delta B_Z > 0$, i.e. the pulse magnetic field acts to increase the background field (see Figure 1). In Equations (2) and (3) f is an arbitrary function of $R + V_0t$ and ϕ . Once a particular form for f and the background field are specified, the particle gyrocenter motion will be explicitly calculated in the pulse and background fields.

We note from Equations (2) and (3) that if either the electric or magnetic “perturbation” field returns to zero after the pulse passes, the other one will return to zero as well. Since we want the pulse to effectively “dipolarize” the background field, the “perturbation” magnetic field should not return to zero after the pulse passes, and we will soon see that this presents a problem of field continuity if one requires the electric field to be zero both before as well as in the wake of the pulse.

2.1. Field continuity for a propagating pulse changing the “background” B-field

One can easily show that an electromagnetic pulse with both perturbed electric/magnetic fields going to zero at the beginning and at the end cannot change the background \mathbf{B} in the wake of the pulse. Let us now allow the background field to be changed by the dipolarization pulse, and thus have a time-dependent form

$$B_{back} = B_{dip} - \frac{\mathcal{B}_c}{R}h(\xi) \quad (4)$$

where B_{dip} is the dipolar field, \mathcal{B}_c is a constant (with dimensions of magnetic field times distance) and $h(\xi)$ an arbitrary function of $\xi = R + V_0t$, the radial argument of the pulse wave function. To have the field stretched before the pulse and dipolar in its wake, let us assume $h(\xi)$ to be a constant before the pulse arrives, and let h change such that after the pulse passes a certain location h becomes zero there, i.e. the background field reverts to dipolar. On this field we want to superpose a “pulse field” in the form $\delta B_Z = \mathcal{E}_0\mathcal{R}(\xi)/(V_0R)$ (we neglect the ϕ dependence for now). We want the function \mathcal{R} above to be zero both in front as well as in the wake of the pulse. Leaving \mathcal{R} an arbitrary function at this point and integrating the Z -component of Faraday’s law for this case [since the “background” magnetic field has a time-

dependence through $h(\xi)$ in this case, there will be an additional term corresponding to it in Equation (1)], we obtain

$$RE_\phi \Big|_{\xi=\xi_f} - RE_\phi \Big|_{\xi=\xi_i} = -\mathcal{E}_0 [\mathcal{R}(\xi_f) - \mathcal{R}(\xi_i)] + V_0\mathcal{B}_c [h(\xi_f) - h(\xi_i)] \quad (5)$$

If now initially (before the pulse arrives at a certain location) we allow in Equation (4) $h(\xi = \xi_i) > 0$ (such that the field is lower than dipolar) and to be a constant (which we incorporate into \mathcal{B}_c , thus setting h to 1) and at the end of the pulse $h(\xi = \xi_f) = 0$ (such that the field reverts to dipolar), one has from the equation above

$$RE_\phi \Big|_{\xi=\xi_f} - RE_\phi \Big|_{\xi=\xi_i} = -V_0\mathcal{B}_c, \quad (6)$$

where we also used $\mathcal{R}(\xi_f) = \mathcal{R}(\xi_i) = 0$ (that is, the pulse has a limited radial extent).

From Equation (6) one sees that if the electric field is zero in front of the pulse, it will be non-zero at the end, and will have a constant (westward) value $-V_0\mathcal{B}_c$! This is counter to observations showing that the westward field after substorm onset is much lower than during the growth phase and about zero on average [e.g., Maynard *et al.*, 1996].

As an aside, we remark that the problem above would not appear if the magnetospheric reconfiguration were to be achieved not by a propagating pulse, but through some other means. For example, if a “global” reconfiguration of the whole magnetosphere is considered, one can set the electric fields at the beginning and at the end of the reconfiguration process to zero [Delcourt *et al.*, 1990]. Nevertheless, such a global reconfiguration is unrealistic for the substorm onset, as it is not consistent with observations [e.g., Liou *et al.*, 2002] showing a clear propagation of a locally-excited dipolarization region. A “global” reconfiguration could, however, an appropriate description of the substorm growth phase, during which magnetic field changes are slow, stretching over a period of up to one hour.

If we wish to describe the dipolarization of the background field as taking place solely through the propagating pulse, then Equation (6) clearly stipulates that we cannot start and end with the same value for the equatorial azimuthal electric field. If we assume that the electric field vanishes after the passage of the pulse, one way around the problem above is to consider a small eastward field at the beginning of the pulse. The need for such an eastward field might appear at this point to be just a mathematical requirement without physical relevance. We note however that the existence of such an eastward field is actually supported by observations. Indeed, CRRES studies [Maynard *et al.*, 1996; Erickson *et al.*, 2000] have shown that the electric field consistently reverses sign from dawn-dusk to dusk-dawn direction for a short period just before the dipolarization (substorm onset) (see Figure 2 of Erickson *et al.* [2000]).

We will therefore study the injection problem by considering a small starting eastward electric field before the pulse. We note that this electric field is not necessarily due to any propagating event, nor is it necessarily inductive, even though it could be related to a magnetosphere-wide reconfiguration of the type studied by Delcourt *et al.* [1990]; Delcourt [2002]. From the point of view of our study (i.e. particle tracing), its exact nature is not relevant. We will also see that this constant \mathbf{E} -field in the front of the pulse has a very small effect on the particle motion.

2.2. Background magnetic field

To obtain the total fields, we superpose the pulse fields upon a new time-dependent, more realistic background magnetic field. This field is chosen by giving a particular value to $h(\xi)$ in Equation (4), and have the form

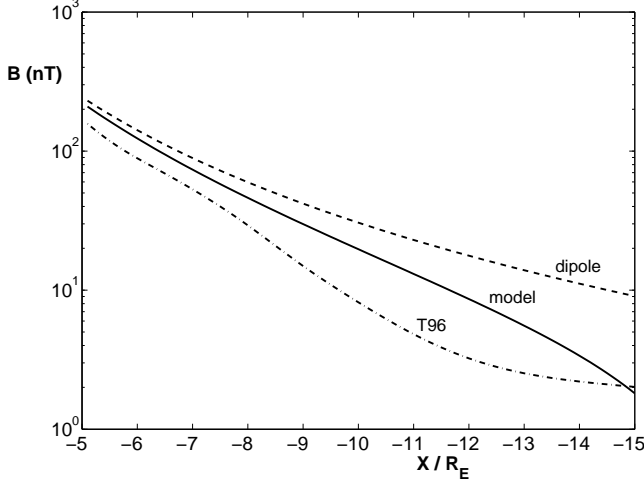


Figure 2. Magnetic field profile along the midnight meridian in the equatorial plane for: dipole (dashed), T96 with $B_{ZIMF} = -5$ nT, $B_{YIMF} = 0$, $P_{SW} = 3.5$ nT and $D_{st} = -5$ nT (dash-dotted) and our new model background field before substorm onset (solid line).

$$\mathbf{B}_0(R, \phi, Z = 0) = \left\{ B_E \left(\frac{R_E}{R} \right)^3 - \frac{\mathcal{B}_c}{R} \cdot [1 - \mathcal{H}(\xi - \xi_2) \frac{\xi - \xi_2}{\Delta_3}] \right\} \hat{\mathbf{z}} \quad (7)$$

where \mathcal{H} is the Heaviside function,

$$\mathcal{H}(x) = \begin{cases} 0 & \text{if } x < 0, \\ 1 & \text{if } x \geq 0, \end{cases} \quad (8)$$

B_E and R_E are the field value at the equator on Earth's surface and the Earth radius, respectively, while as mentioned $\mathcal{B}_c > 0$ is a constant and ξ is the radial argument of the wave function, $\xi = R + V_0 t$ (indicating the “phase” of the dipolarization wave). The other two quantities are ξ_2 , indicating a certain position on the wave form in front of which ($\xi < \xi_2$) the background field is stretched (lower than dipolar), and in the wake of which ($\xi > \xi_2$) the field relaxes to dipolar. As the dipolarization wave moves Earthward, the point of constant ξ_2 moves towards lower R values, thus reverting the \mathbf{B} -field everywhere to a dipolar state. The dimensional constant Δ_3 determines the length scale over which the background field reverts to dipolar values in the wake of the pulse. The formula above is only valid for $\xi \leq \xi_2 + \Delta_3$ (at equality, the background field has completely reverted to dipolar, and will remain so for larger values of ξ).

As in our previous work, the actual value of B_E will be adjusted (usually to be lower than the value of the field at the Earth's surface) to include the diamagnetic effect of the ring current, since all particles in our study are at locations farther away than the ring current region. The actual choices for both B_E and \mathcal{B}_c will be in accord with magnetic field observations.

While certainly the portrayal of the reduced background field through Equation (7) is a simplification vs. the more complex, three-dimensional field structure during the growth phase [Zaharia and Cheng, 2003a], a judicious choice of \mathcal{B}_c will allow us to model a very important feature from the point of view of particle motion, which is the sharp difference between the stretched and the dipole fields. Thus, the

consideration of a tail-like background field in the present study is a significant improvement of the particle transport model. A field of the form in Equation (7) is more realistic [Schulz and Chen, 1995] than a simple dipole field especially for applications related to describing particle access into the inner magnetosphere from the plasma sheet. While Schulz and Chen model (for a different purpose) the background field by subtracting a constant southward term, we subtract a term that decreases with distance. The form of the subtracted term ensures that close to Earth, while the term is larger, it is still very small compared to the overwhelming Earth dipole field, while farther away the relative ratio between the subtracted term and the dipole value increases, consistent with observations showing the field being more and more different from a dipole field with increasing distance from Earth. Both our choice and the choice of Schulz and Chen [1995] give rise to a “Dungey” appearance for the background magnetic field. Our new model background field with the above value for \mathcal{B}_c is more realistic than a dipolar field, as shown in Figure 2. However, the figure also shows that it only conservatively models the stretching: while the model field is drastically stretched vs. the dipolar field, it is not as stretched as the T96 field for example in the region closer than $15 R_E$ from Earth. Furthermore, the T96 field, being a statistical field obtained from many observations at different times, may not be itself stretched enough to represent the pre-onset field.

While the field portrayed in Equation (7) formally corresponds to a neutral line (where $B_0 = 0$) at $R_X = \sqrt{B_E R_E^3 / \mathcal{B}_c}$, that will occur at a distance farther away from Earth than our region of interest (with the parameters defined such that the subtracted field is a fraction $f = 0.8$ of the dipole field at $15 R_E$, $R_X = 15 / \sqrt{f} \approx 16.8 R_E$). We note however that the topology of the model field is probably not too realistic at larger distances (farther than $15 R_E$), as the term subtracted from the dipole field does not decrease fast enough there. However, this fact need not concern us, as our region of interest, to be seen shortly, is well inside $15 R_E$ from Earth.

2.3. Dipolarization wave field

The actual shape of the pulse form in the (ξ, ϕ) coordinates needs to be chosen now in order to proceed. Following

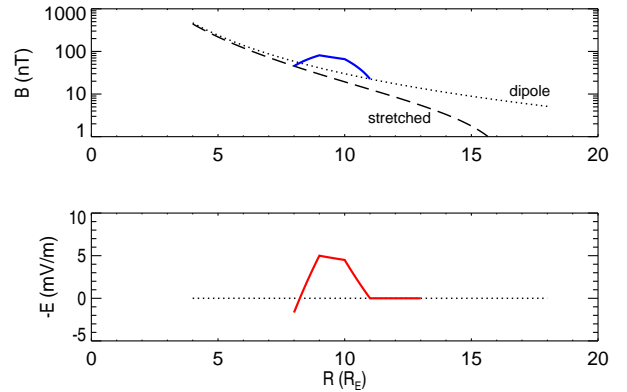


Figure 3. Profiles as a function of distance R at an instance in time for: (top) Total magnetic field in the pulse region (solid blue), tail-like background field (dashed) and dipolar (dotted). The background magnetic field is tail-like in front of the pulse and relaxes to a dipolar configuration in its wake. (bottom) Electric field of the pulse (solid red), starting with a small eastward component in front of the pulse and vanishing in its wake.

our previous discussion above and considering an azimuthal dependence $\Phi(\phi)$ in the pulse quantities as well, we choose a “pulse” magnetic field and \mathbf{E} -field starting from a non-zero, positive (i.e. eastward) value before the onset, in the forms:

$$R\delta B_Z = \frac{\mathcal{E}_0}{V_0} \mathcal{R}(R + V_0 t) \Phi(\phi) \quad (9)$$

$$RE_\phi = \begin{cases} [V_0 \mathcal{B}_c - \mathcal{E}_0 \mathcal{R}(R + V_0 t)] \Phi(\phi) & \text{if } \xi \leq \xi_2, \\ -(\mathcal{E}_0 - V_0 \mathcal{B}_c) \mathcal{R}(R + V_0 t) \Phi(\phi) & \text{if } \xi > \xi_2 \end{cases} \quad (10)$$

where \mathcal{E}_0 is a constant, familiar from our previous study, with dimensions of distance times electric field, \mathcal{B}_c is the constant introduced in the previous section that decreases the value of the background field, $\Phi(\phi)$ is a function representing the azimuthal dependence of the pulse fields, while $\mathcal{R}(R + V_0 t)$ is the same three-part trapezoidal radial wave form used before (see Figure 3 of [Zaharia et al., 2000]), normalized to unity at the maximum pulse amplitude:

$$\mathcal{R}(\xi) = \begin{cases} \frac{\xi - \xi_0}{\Delta_1} & \text{if } \xi_0 \leq \xi \leq \xi_1 = \xi_0 + \Delta_1, \\ 1 & \text{if } \xi_1 \leq \xi \leq \xi_2 = \xi_1 + \Delta_2, \\ 1 - \frac{\xi - \xi_2}{\Delta_3} & \text{if } \xi_2 \leq \xi \leq \xi_3 = \xi_2 + \Delta_3 \end{cases} \quad (11)$$

It is easy to verify that the electric field given by Equation (10) starts from an eastward value at the beginning of the pulse and becomes zero in its wake. In Figure 3 we plot as a function of R both the total magnetic field [the “pulse” field given by Equation (9) superposed on the background field defined in Equation (7)], as well as the electric field at a certain time (a “snapshot” during the pulse motion). We note that the actual shape of the pulse fields is not exactly the shape of \mathcal{R} , because of their dependence as $1/R$ required by energy conservation as the pulse propagates inward [Zaharia et al., 2000]. Since we only consider the problem in the equatorial plane, we have no Z -dependence and $\nabla \cdot \mathbf{B} = 0$ is trivially satisfied by the combined pulse + background magnetic fields.

Looking at the top plot in Figure 3, one observes that in the front of the pulse the background magnetic field is lower than the dipolar field, but the pulse “fills in” the magnetic field difference as it arrives at a certain location. We note that for the particular choice $\mathcal{E}_0/V_0 = \mathcal{B}_c$, at the maximum amplitude $\mathcal{R} = 1$ the pulse completely “fills in” the difference between the dipole and the stretched magnetic fields. Such a pulse however would have quite low transient fields, and in fact much higher fields have been observed during substorms [Shepherd et al., 1980; Aggson et al., 1983]. Therefore in our study we will choose \mathcal{E}_0/V_0 significantly larger than \mathcal{B}_c , such that there will be a significant “overshoot” past the dipole field value toward the late stage of the first part of the pulse. Such a choice will also ensure that the eastward field at the beginning is much smaller than the pulse field, thus making the effect of the former on the particle motion negligible. Introducing the parameter $\epsilon = V_0 \mathcal{B}_c / \mathcal{E}_0$, the above choice means ϵ significantly less than 1.

In the second part of the pulse the function \mathcal{R} is constant and equal to 1, corresponding to a “saturation” effect limiting the pulse amplitude (such saturation is expected considering the non-linear nature of the pulse). Finally, in the third part of the dipolarization pulse the transient electric field slowly decreases to zero, while the magnetic field decreases, but not to the initial background field (which was the stretched field during the growth phase), but to a dipolar configuration. As mentioned, the decrease of the electric field to zero is consistent with observations [Maynard et al., 1996] showing the electric fields approximately zero on average after the substorm.

With regard to the azimuthal dependence, in this paper we will again as before restrict the pulse fields to be localized within a “wedge” of azimuthal extent $2\delta\phi$ (see Figure 2

in [Zaharia et al., 2000]), and zero outside, however we allow the wedge to be centered at an arbitrary position ϕ_0 , not necessarily $\phi_0 = 180^\circ$ (midnight) (observational studies have found that in many cases the dispersionless injection events are slightly skewed towards dusk [e.g., Friedel et al., 1996; Birn et al., 1997a]):

$$\Phi(\phi) = \begin{cases} 1 & \text{if } \phi_0 - \delta\phi < \phi < \phi_0 + \delta\phi, \\ 0 & \text{otherwise} \end{cases} \quad (12)$$

Such a “sharp” form for the azimuthal dependence of the pulse fields is chosen mainly for reasons of simplicity; however we note that observations [e.g., Friedel et al., 1996] do show that the region of dispersionless injection can have sharp boundaries in magnetic local time.

2.4. Particle motion; adiabaticity

We will solve the non-relativistic particle gyrocenter equation of motion in the electric and magnetic fields of the pulse plus background field. The proton and electron motions conserve the magnetic moment as before [Zaharia et al., 2000], a fact valid here for distances less than $12 R_E$ (where our new model background field reaches 10 nT), due to the spatial and temporal scales involved. To illustrate this, we note that, for example, a 400 keV proton has a gyro-radius of about 66 km in a 10 nT field, a value much smaller than any spatial scales in our study. For electrons, the first adiabatic invariant conservation is even stronger: an electron of 400 keV has a gyro-radius in the same field of only about 1 km. We note here that, as opposed to electrons and protons, heavier ions such as O+ might become non-adiabatic [e.g., Delcourt, 2002]; however they are not the object of the present study.

Like previous studies [Li et al., 1998; Zaharia et al., 2000; Sarris et al., 2002], we will only take into account 90° pitch angle particles (with $v_{\parallel} = 0$), i.e. particles confined to the equatorial plane. The particle trajectory can then be found by integrating the gyrocenter equation of motion:

$$\mathbf{V}_{\text{gc}} = \frac{d\mathbf{r}}{dt} \quad (13)$$

$$= \mathbf{V}_{\mathbf{E} \times \mathbf{B}} + \mathbf{V}_{\nabla B}, \quad (14)$$

where

$$\mathbf{V}_{\mathbf{E} \times \mathbf{B}} = \frac{\mathbf{E} \times \mathbf{B}}{B^2}, \quad (15)$$

$$\mathbf{V}_{\nabla B} = \frac{\mu}{qB^2} \mathbf{B} \times \nabla B, \quad (16)$$

q is the particle charge and $\mu = mv_{\perp}^2/(2B)$ represents its magnetic moment. Equation (16) is the non-relativistic form of the ∇B drift. The non-relativistic theory can be applied to proton injections in a wide range of events and may also be used to approximate electron motion for energies lower than the electron rest energy (511 keV). There is no curvature drift in (14) because we only consider particles with $v_{\parallel} = 0$; the polarization drift can also be neglected, as explained before [Zaharia et al., 2000], for particles with thermal speeds above the pulse velocity V_0 (i.e. proton energies above about 100 eV, certainly the case in this study).

A particle moving adiabatically in the fields of the pulse is energized by the betatron acceleration process, such that

the change in energy only depends on the magnetic field values at the initial and final positions of the particle, with the final energy being given by [Zaharia *et al.*, 2000]

$$W = W_0 \frac{B_f}{B_i}, \quad (17)$$

where W_0 is the energy at the initial position \mathbf{r}_0 with magnetic field B_i , while B_f is the total magnetic field at the final position \mathbf{r} after interaction with the pulse.

One can surmise that betatron acceleration with initial background field lower than dipolar will produce higher particle energies compared to the case when the background field is a dipole, if the transport is roughly the same. This is because the ratio of the fields at the particle's final vs. initial locations is larger in this case. While the energization mechanism has the potential to be stronger in this case, it remains to be seen how effective the transport is compared to the case of a dipolar field. In order to ascertain this, we will explore in detail in the following the gyrocenter motion in the given pulse plus background fields, presenting completely analytical solutions for the particle trajectories.

2.5. General radial solutions

For $\xi \leq \xi_2$, the background magnetic field has a time-independent “tail-like” configuration. Therefore, as long as the particle is not in the third part of the pulse (where $\xi > \xi_2$) one can write the radial equation of motion for its gyrocenter (given by the $\mathbf{E} \times \mathbf{B}$ drift) as

$$\frac{dR}{dt} = -V_0 \cdot \frac{\mathcal{E}_0 \mathcal{R}(R + V_0 t) - V_0 \mathcal{B}_c}{V_0 B_E R_E \left(\frac{R_E}{R}\right)^2 - V_0 \mathcal{B}_c + \mathcal{E}_0 \mathcal{R}(R + V_0 t)} \quad (18)$$

Equation (18) can be integrated for an arbitrary shape of \mathcal{R} , to give the solution

$$\frac{1}{R} - \frac{1}{R_i} = \frac{\mathcal{E}_0}{V_0 B_E R_E^3} \int_{\xi_i}^{\xi} \mathcal{R}(\xi) d\xi - \frac{\mathcal{B}_c}{B_E R_E^3} (\xi - \xi_i) \quad (19)$$

where $\xi_i = R_i + V_0 t_i$, $\xi = R + V_0 t$, R_i is the initial radial position at time t_i (when the particle encounters the pulse) and R is the position at time t in the pulse. Equation (19) gives the solution explicitly in the form $R = R(\xi)$; however $\xi = R + V_0 t$ and thus the solution can be expressed as $R(t)$ as well.

The radial transport is seen to be decreased here (for the same \mathcal{E}_0) compared to our previous study, due to the subtracted term proportional to $\mathcal{B}_c(\xi - \xi_i)$ in Equation (19), which appears because of the lowered electric field.

Equation (19) is only valid for the first and second parts of the dipolarization pulse. For the third part of the pulse (which is superposed on the time-varying background \mathbf{B} -field, as given by Equation (7) for $\xi > \xi_2$), the radial equation of motion is different:

$$\frac{dR}{dt} = -V_0 \cdot \frac{(\mathcal{E}_0 - V_0 \mathcal{B}_c) \mathcal{R}(R + V_0 t)}{V_0 B_E R_E \left(\frac{R_E}{R}\right)^2 + (\mathcal{E}_0 - V_0 \mathcal{B}_c) \mathcal{R}(R + V_0 t)} \quad (20)$$

It is clear that Equation (20) is equivalent to the expression found before for the motion in a pulse superposed on a dipolar field (with $\mathcal{E}_0 - V_0 \mathcal{B}_c$ replacing \mathcal{E}_0 in Equation (12) of [Zaharia *et al.*, 2000]), and has the solution

$$\frac{1}{R} - \frac{1}{R_i} = \frac{\mathcal{E}_0 - V_0 \mathcal{B}_c}{V_0 B_E R_E^3} \int_{\xi_i}^{\xi} \mathcal{R}(\xi) d\xi \quad (21)$$

The general-form radial solutions just presented are then applied to our particular case of a trapezoidal pulse. Analytical solutions are found for both the radial and azimuthal equations of motion in the pulse and background fields. The full solutions, similar in form to the ones previously obtained for the case of a dipole background [Zaharia *et al.*, 2000], are presented in the Appendix.

2.6. Injected particle flux

With the particle orbits found analytically, the next step is computing the “injected” particle flux. We will briefly outline here the details of this computation. As discussed before [Zaharia *et al.*, 2000], because we only consider 90° pitch-angles we will only be able to compute the directional flux j [Roederer, 1970] for these particles. Comparison between this flux obtained from the model and the observed omni-directional flux J can be made if we assume that particles with other pitch angles are energized in the same degree, i.e. $J = 4\pi j$ (a discussion of this assumption will be made in the last section of the paper).

Using Liouville's theorem of conservation of phase space density along the particle trajectory, one can easily obtain the flux j at location (R, ϕ) for particles with initial energy W_i that were energized to energy W , in the form [Zaharia *et al.*, 2000]

$$j = \frac{W}{\pi \sqrt{W_i}} \left(\frac{1}{2m}\right)^{3/2} f(W_i, R_i, \phi_i, t_i) \quad (22)$$

where $f(W_i, R_i, \phi_i, t_i)$ is the distribution function (in energy) at the initial particle location (R_i, ϕ_i) , while m represents the particle mass. The expression above can easily be evaluated since for adiabatic motion the final particle energy is only a function of the initial energy and the ratio of the magnetic fields at the particle's final and initial locations, respectively: $W = W_i B(R, \phi, t) / B(R_i, \phi_i, t_i)$.

3. Particle Transport and Energization

Our main goals in this Section are to ascertain the magnitude of the particle transport/energization, to explain certain observed features of the injections (such as the displacement between protons and electrons and the low- and high-energy cutoffs), and to see how different the results are for our present computation with a more realistic background field vs. the previous case of a dipolar field.

3.1. General discussion of the particle motion

As discussed before [Zaharia *et al.*, 2000], in our pulse model one can separate four distinct classes of particles interacting with the pulse. We will discuss this classification in more detail here. Typical trajectories of electrons of each of the four types, all arriving to geosynchronous orbit but from different initial positions, are presented in Figure 4.

In each plot in the figure, point A represents the particle entrance into the pulse, while point B the exit. The trajectory while in the pulse is in color (red for the first part of the pulse, and green and blue, respectively, for the second and last part of the pulse). The first kind of particles are those that (in the pulse frame of reference) both enter and leave the pulse radially. Because they stay in all three parts of the pulse, these particles (we call them type I) travel the largest radial distance (see Figure 4) and their energization is the

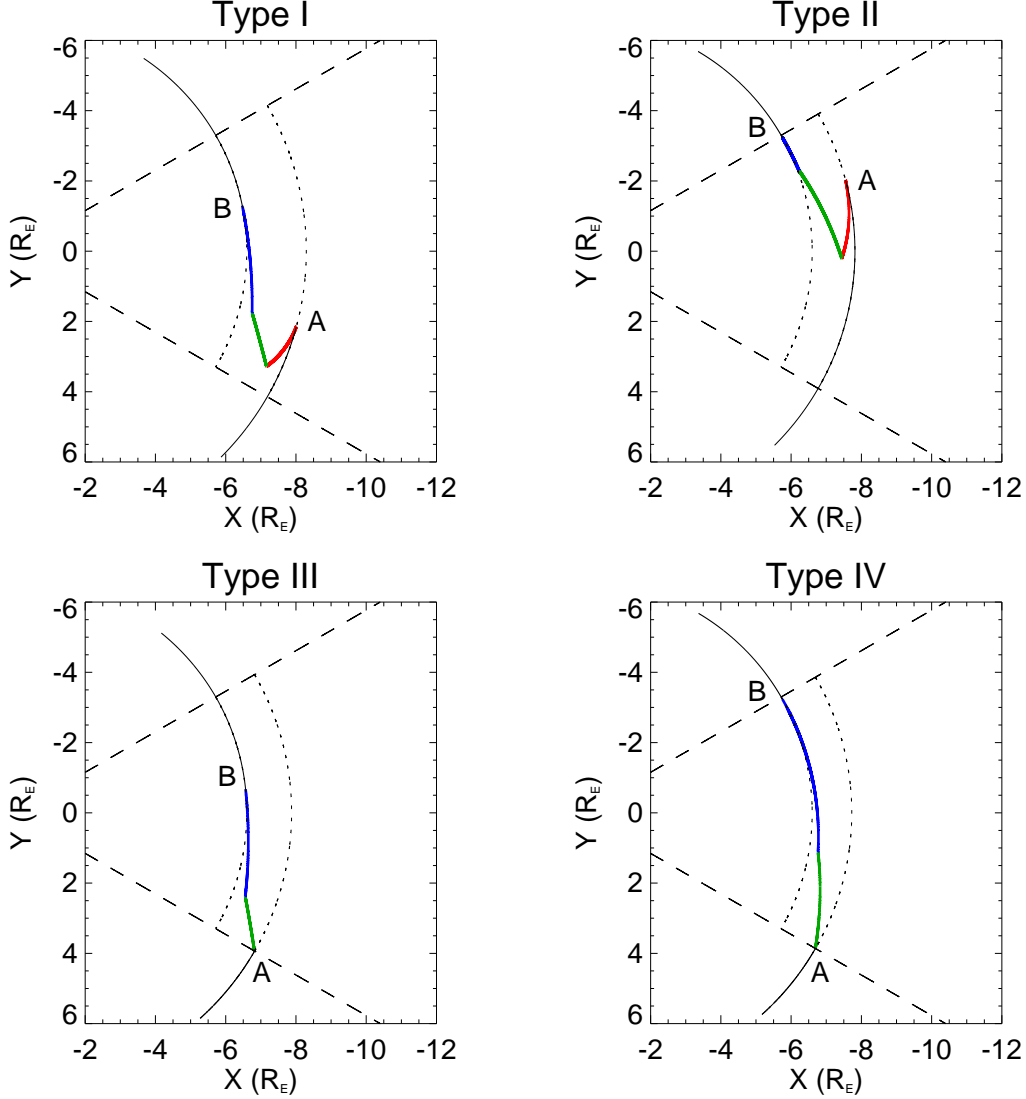


Figure 4. Typical gyrocenter trajectories of electrons of each of the four types. The motion while in the pulse is shown in color (red for the first part of the pulse, and green and blue, respectively, for the second and last part of the pulse). The drift before entering the pulse and after exiting it is shown in thin solid black lines. The pulse and background parameters are those given in Section 3.2. The type-I electron shown has the largest radial transport, from the initial distance of $8.29 R_E$ to $6.6 R_E$, and therefore the largest energization. The electrons of types II, III and IV have closer initial distances in order to arrive at geosynchronous, as their radial transport is weaker.

strongest. The energetic flux enhancement at a geostationary observation point will be mainly due to these particles, if their energy is not too high and the pulse not too narrow. Type II particles enter the pulse radially (through its first part) but leave it azimuthally; many high-energy particles fall into this category, as their fast azimuthal drift prevents them from being able to remain in all regions of the pulse (and thus to be of type I). In Figure 4, the type-II electron shown exits the pulse azimuthally while still in its third part, thus not experiencing the maximum energization. The third class of particles are those that enter the pulse azimuthally, but are not very energetic, such that they are able to remain throughout the rest of the pulse and leave it radially at the end of the third part. These particles would probably have been type-I, had they been inside the local-time “wedge” of the pulse when the pulse arrived at their radial coordinate. The type-III electron shown in Figure 4 entered the pulse azimuthally at the beginning of the second part and there-

after stayed in all of parts 2 and 3 of the pulse, however its radial transport is lower than for type-I because it “missed” the first part of the pulse. Finally, the last class of particles (type IV) both enter and exit the pulse azimuthally — these again are likely to be higher-energy particles. In Figure 4 the type-IV particle shown, entering the pulse also at the beginning of the second part, experiences the least radial transport, as its large azimuthal drift did it to stay in all of the third part of the pulse.

While the particle motion is not very different from the one previously obtained [Zaharia *et al.*, 2000] (for a type-I proton gyrocenter trajectory in the fixed reference frame tied to Earth, see Figure 5 of [Zaharia *et al.*, 2000]), it is interesting to note quantitative differences between the two cases. We will look at type I particles, which experience the largest degree of energization and will thus likely make up the bulk of injected particles. For those we can derive a simple analytical formula for their final radial exit position R_3 as a function of the initial position R_0 . Indeed,

combining Equations (A1), (A4) and (A6) (presented in the Appendix) for the radial motion in the three parts of the pulse, we obtain

$$R_3 = \frac{R_0}{1 + \frac{\mathcal{E}_0 R_0 [\Delta_1 + 2\Delta_2 + \Delta_3 - \epsilon(2\Delta_1 + 2\Delta_2 + \Delta_3)]}{2V_0 B_E R_E^3}} \quad (23)$$

Now if we wish to compare the current case with the previous study, it makes sense to compare events with the same pulse amplitude of the electric field. The maximum amplitude in this case is characterized by $\mathcal{E}'_0 = \mathcal{E}_0 - V_0 \mathcal{B}_c = \mathcal{E}_0(1 - \epsilon)$, and by re-writing Equation (23) to show \mathcal{E}'_0 explicitly and inverting it to have the initial location R_0 as a function of the final location R_3 we obtain

$$R_0 = \frac{R_3}{1 - \frac{\mathcal{E}'_0 R_3 [\Delta_1(1 - \epsilon) + 2\Delta_2 + \Delta_3]}{2V_0 B_E R_E^3}} \quad (24)$$

If \mathcal{E}'_0 is considered to be the equivalent of \mathcal{E}_0 used before [Zaharia *et al.*, 2000], the only difference in the radial transport for the present case is the $1 - \epsilon$ factor in the expression above. Since ϵ is significantly less than 1, it follows that the radial transport is only slightly lower than before, and the difference is entirely due to the motion in the first part of the pulse. The motions in the second and third parts are characterized by exactly the same degree of radial transport (again, with the assumption of identical \mathbf{E} -field amplitudes). We also see that for $\epsilon \ll 1$ the particle radial transport, as before, only depends on the electric field parameter \mathcal{E}_0 and the pulse velocity V_0 through their ratio \mathcal{E}_0/V_0 .

3.2. Parameter choices

In order to be more quantitative in describing various features of the transport and energization processes we need to choose values for the pulse/background field parameters and specify the particle distribution. All these parameters will be chosen to have typical values consistent with observations, with justification given for each choice.

One very important quantity, the pulse velocity V_0 , is found by different observations to have rather different values. Perhaps the first direct observation of dipolarization pulse speed was made by Russell and McPherron [1973] using a favorable alignment of the OGO-5 (located at $8.4 R_E$ from Earth in the equatorial plane) and ATS-1 spacecraft (at $6.3 R_E$), both near the midnight meridian. Russell and McPherron clocked the time delay between the field increase at the each spacecraft to be 94 s, resulting in a propagation velocity for the dipolarization wave of 143 km/s. An even higher Earthward velocity (270 km/s) at geostationary orbit for the dipolarization front was found by Liou *et al.* [2002] by analyzing the delay between *in situ* measurements of magnetic fluctuations and auroral breakup observations. Inside the geosynchronous orbit however, observations by Reeves *et al.* [1996] found the propagation speed of injections to be much slower (24 km/s). Finally, we note that Moore *et al.* [1981] report plasma flow velocities in the region from 9 to $6 R_E$ of between 10 and 100 km/s. In our model, the plasma radial flow velocity, given by the $\mathbf{E} \times \mathbf{B}$ drift, is necessarily lower than the pulse speed (the pulse always moves faster than any particle dragged by it). We will attempt a compromise among the above observations by choosing a pulse velocity of 125 km/s in our domain of interest ($R > 6.6 R_E$).

The rather large radial propagation velocity also warrants neglecting the azimuthal expansion of the pulse, which is however an observed effect [e.g., Belehaki *et al.*, 1998; Thomson *et al.*, 2001]. Indeed, the observations by Belehaki *et al.*

[1998] of the longitudinal expansion of the dipolarization signature find a small angular azimuthal velocity, of less than $1^\circ/\text{min}$, corresponding to 16 km/s at $9 R_E$ and 12 km/s at geostationary orbit, which is small enough compared to the observed radial velocities that it can be neglected as a first approximation, as for a pulse with a radial velocity of 125 km/s it takes about 3 min to propagate $3.4 R_E$ between $10 R_E$ and geosynchronous orbit, and during this time there will be an increase in its azimuthal width of less than 3.4° (which has to be compared to 60° , or about 6 hours in local time, the typical azimuthal width of the pulse).

For the dipole magnetic field value we choose $B_E = 0.22 \text{ G}$, a value lower than the actual field at the Earth's surface, in order to include the diamagnetic effect of the ring current. Another important parameter is the quantity \mathcal{B}_c , which lowers the background magnetic field during the substorm growth phase (before the arrival of the pulse). In view of our discussion in the Introduction, we will choose for \mathcal{B}_c a value such that the magnetic field subtracted from the dipole field at $15 R_E$ would be 80% of the dipole field there: $\mathcal{B}_c = 0.8 B_E R_E^3 / (15 R_E)^2$.

For the other pulse parameters, typical values are $\mathcal{E}'_0 = 5 \text{ mV/m} \cdot 9 R_E$, $\Delta_1 = \Delta_2 = \Delta_3 = 1 R_E$, and $2\delta\phi = 60^\circ$ (a typical width of the “substorm current wedge” [e.g., Clauer and McPherron, 1974]). With the chosen values for the electric field and the difference in the background magnetic field, we have $\epsilon = V_0 \mathcal{B}_c / \mathcal{E}_0 = 0.18$. With regard to the particle distribution, we will model it as before by a kappa distribution in energy [Vasyliunas, 1968]:

$$f(W, R) = f_0 \cdot g(R) \cdot \left[1 + \frac{W}{(\kappa - 1.5)\epsilon} \right]^{-\kappa - 1} \quad (25)$$

with ϵ being the average energy (not to be confused with $\epsilon = V_0 \mathcal{B}_c / \mathcal{E}_0$), κ a parameter and f_0 a constant. To model a moderately active plasma sheet we choose for protons $\kappa = 6.5$ and $\epsilon = 7 \text{ keV}$ in our region of interest ($6.6 R_E$ to $10 R_E$). For electrons we choose $\kappa = 4$ and $\epsilon = 2 \text{ keV}$ as before [Zaharia *et al.*, 2000]. These values are similar to values obtained by Christon *et al.* [1991] and also used by Birn *et al.* [1997b]. The radial dependence $g(R)$ is also taken as before in the form $g(R) = (R/R_E - 3)^4 / (R/R_E)^{10}$, also used by Li *et al.* [1998]. The particle distribution is assumed to be uniform in local time.

3.3. Strength of particle transport and energization

With the chosen parameters, we study the strength of radial transport and energization for both protons and electrons. In this section we will only analyze type-I particles (i.e. those that enter and exit the pulse radially, and therefore are energized the most). We will also try at each step to make a comparison with the previous case with a dipole background, with the same pulse parameters (that case can be simply recovered by putting $\mathcal{B}_c = 0$, and therefore $\epsilon = 0$ and $\mathcal{E}' = \mathcal{E}$ in the equations derived so far).

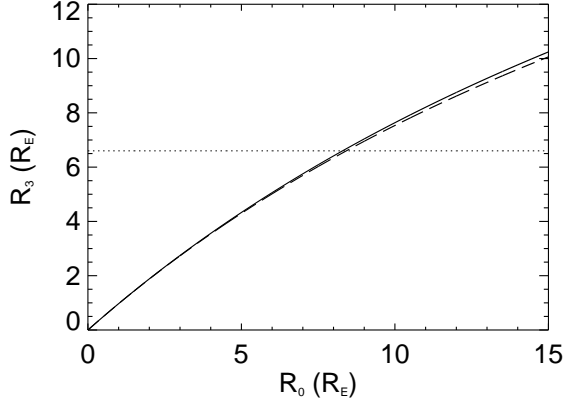


Figure 5. Final distance R_3 versus initial radial distance R_0 for particles entering and exiting the pulse radially; the solid line shows the new case with non-dipolar time-dependent background field, while the dashed line the old case with dipole background. The dotted horizontal straight line shows the geosynchronous location.

Using Equation (24) we find that for the present case the initial distance from where a particle (proton or electron) is injected to geostationary orbit is $8.29 R_E$, compared to $8.42 R_E$ that would be obtained using the previous model. This difference, amounting to 1.5%, is, as expected, a very small change in the radial transport, and appears due to lower transport in the first part of the pulse in the present case. In fact, for any initial distance up to $15 R_E$, the final particle distance, as seen in Figure 5, is not much different for the new case compared to the previous one.

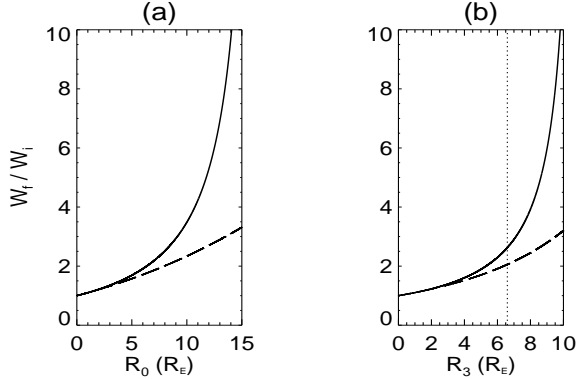


Figure 6. Ratio of final to initial energy W_f/W_i for injected particles in the current model (solid) and the previous model (dashed), plotted as a function of (a) initial position R_0 and (b) final position R_3 ; the dotted vertical line in the final graph shows the geosynchronous location.

While the radial transport of the particles is only very slightly affected (decreased) compared to the case treated before, their energization is significantly larger in the present model. To illustrate this, in Figure 6(a) we plot the ratio of final to initial energies, W_f/W_i , computed using each of the two models, against the initial position the particles arrive from. For particles with initial positions farther than about $5 R_E$ from Earth, it is evident that the energization they undergo is much larger for the present model than for the previous case with dipolar background field. Since the radial transport is about the same, the increase is almost

entirely due to the much different ratio between final (dipolar) vs. initial (stretched in this case) background magnetic fields. In Figure 6(b) we show the same ratio W_f/W_i , this time plotted against the final (injected) particle location. For injections to geosynchronous orbit ($R_3 = 6.6 R_E$), the ratio of final vs. initial energies is 2.63 for the present model, while for the model with dipolar background the ratio is only 2.07. This increase of 27% is a rather marked change, and for injections to farther distances the difference can become dramatic, as seen in Figure 6(b). Such differences will translate into orders of magnitude differences in the injected flux, due to the highly-nonlinear nature of the kappa distribution, as we will see shortly.

3.4. Injected flux increase

For the chosen pulse and particle distribution parameters, we now analyze the increase in flux for the most energized particles, i.e. type-I, which stay in all parts of the pulse. While the radial transport is the same for protons and electrons (the $\mathbf{E} \times \mathbf{B}$ drift is the same), the injected flux increase will be different for electrons vs. protons, due to their different kappa distributions, and we will therefore treat them one at a time. First, let us look at protons. The top plot of Figure 7 shows the injected/background proton flux ratio for a large range of “substorm energies”, while the bottom plot concentrates on lower energies from 1 to 50 keV. The solid lines show the results with the new model, while the dotted lines the results with the old model with dipolar background. Analyzing the two plots one observes that for all energies larger than 30 keV both the old and the new models predict that the increase in fluxes exceeds an order of magnitude, with flux ratio approaching 1000 with the new model for an energy of 400 keV, and even larger for higher energies. This dramatic increase is a consequence of the kappa distribution, which rapidly decreases with increasing particle energy for energies much larger than the average population. For the injected particles, their number is given by the distribution at their origin (where they had a lower energy), and it is to be compared to the very small “background” population for the higher energy at the injection location.

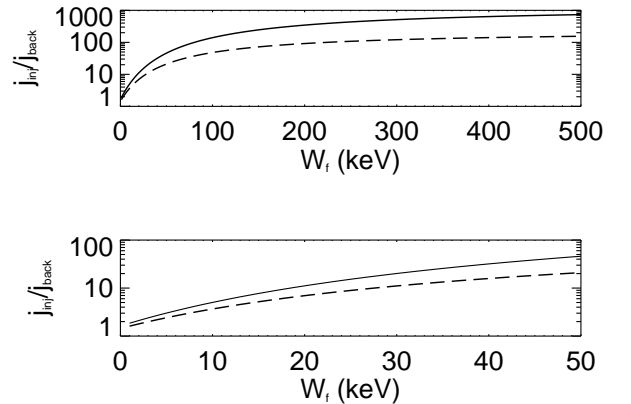


Figure 7. Ratio j_{inj}/j_{back} of injected vs. background flux for protons transported to geostationary orbit, as a function of their energy W_f at the injection point, for the new model (solid) as well as the old model (dashed). The top plot shows a wide range of energies, while the bottom plot concentrates on a lower energy range.

The flux increase is seen to be significantly larger (one order of magnitude in most of the energy range) for the new

model vs. the old model, as expected due to the higher energization and the non-linear nature of the kappa distribution. The bottom plot in Figure 7 shows that for energies lower than 50 keV, the flux increase is dramatically lower than for the “substorm energies”, thus providing an explanation for the “cutoff” seen at low energies in substorm injections [Reeves, 1998]. The lower flux increase is due to the fact that for low energies the kappa distribution does not vary dramatically with energy, thus explaining the low flux increase for this population, compared to the dramatic increase for higher energies. From Figure 7 we can infer however that for a typical event this cutoff is below 50 keV, as protons in the 50 keV range still experience more than a factor of 10 increase in the injected/background flux ratio.

Our model also explains the high-energy cutoff, also seen in observational studies [e.g., Baker *et al.*, 1979], as a feature of the limited azimuthal extent of the pulse. For electrons, we first note that our non-relativistic treatment does not apply for energies larger than the electron rest energy. For both protons and electrons, however, we will have an “azimuthal cutoff”, due to the local-time extent of the pulse [Zaharia *et al.*, 2000]. For energies larger than the cutoff energy, there will be no type-I particles, and therefore the treatment in this section will not apply. While particles of the other 3 types will be energized by the pulse, they will be transported radially less than the type-I particles and therefore energized less than inferred here. The azimuthal cutoff energy depends on the width of the pulse: for the chosen parameters (including the typical azimuthal width of 60°) the cutoff will be for 440 keV. For a larger pulse of 100° , the cutoff will be higher, at 735 keV. For protons only, we also note that for very high energies, our adiabatic assumption breaks down as the protons do not conserve their magnetic moment anymore, resulting in lower energization than the betatron acceleration mechanism suggests [Birn *et al.*, 2003]. We note as well that analyzing the azimuthal motion in conjunction with the observed high-energy cutoff also allows us to specify constraints on the azimuthal width of the pulse (in conjunction with other pulse parameters).

Finally, let us look at the flux increase for type-I electrons, which will be different from the one for protons due to the different particle distribution. Figure 8 shows the injected flux to background flux ratio j_{inj}/j_{back} at geosynchronous orbit for electrons vs. their energy there.

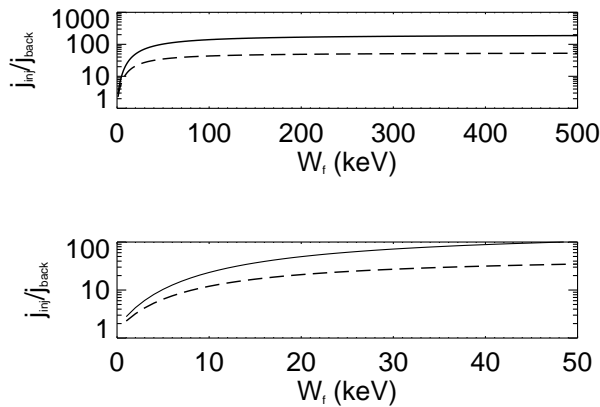


Figure 8. Same as Figure 7, but for electrons.

The figures for protons and electrons are similar, however with some notable differences due to the different kappa distributions. The first difference is the lower flux increase for electrons in the “substorm energy range” (100 to 400 keV)

compared to protons, due to the lower value of κ for electrons. The results with the new model in this case are again quite different from the ones using the old model. In particular, it is seen that with the old model the electron flux increase is capped at a value of about 55; therefore, the old model with the chosen parameters cannot explain injections where the fluxes increase by almost two orders of magnitude; however the new model can. Looking at the low energy range now (1 to 50 keV), we see that for electrons in this energy range the flux increase is higher than for protons, again a feature of their different kappa distribution. The flux increase for the lower energy range is still much less than for substorm energies, and the model thus predicts a low-energy “cutoff” for electrons as well; however this cutoff will be at a lower energy than for protons.

3.5. Azimuthal displacement of proton vs. electron injections

An important aspect of the substorm injections is revealed by observations [Reeves *et al.*, 1990; Birn *et al.*, 1997a; Thomsen *et al.*, 2001] finding that proton and electron injections do not occur in identical regions, but instead are displaced against each other in the azimuthal direction. This feature can be analyzed by looking at our analytical solutions for the particle motion. As they make up most of the injected flux, we will again only study in this section type-I particles, those that stay in all three parts of the pulse. While the radial transport of protons and electrons is the same, their azimuthal drifts are in different directions. The azimuthal displacement between the proton and electron injections is then simply given by the sum of the difference in each part of the pulse:

$$\phi_e - \phi_p = \sum_{j=1}^3 (\phi_{ej} - \phi_{pj}), \quad (26)$$

where ϕ_{ej} and ϕ_{pj} are given (for the corresponding q) in analytical form in Equations (A3), (A5) and (A8).

Considering an electron and a proton carried by the pulse that start from the same initial location and are injected at $6.6 R_E$ with a final energy of 100 keV there, for the chosen parameters the electron will have a net eastward azimuthal drift of 18° , while the proton will have exactly the opposite drift, in the westward direction. Therefore, the total displacement between the proton and electron injections, when only type-I particles are considered, is about 36° , corresponding to a difference in local time of roughly 2 hours. This is a slightly larger value than observations suggest, however we note that particles of other types than type I could have both smaller and larger deflections, and one would need to consider all the types to obtain a more accurate answer.

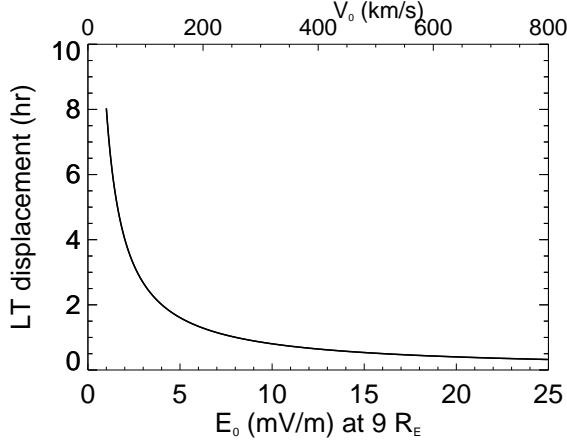


Figure 9. Azimuthal displacement between type-I electrons and protons injected at $6.6 R_E$ with energy 100 keV as a function of \mathbf{E} -field value at $9 R_E$ (lower X -axis) and pulse velocity (upper X -axis), for a constant ratio between the two.

In order to see how the electron/proton azimuthal displacement depends on various parameters of the pulse, in Figure 9 we show the dependence of the displacement for type-I particles as a function of different values of electric field and velocity, but keeping the ratio \mathcal{E}_0/V_0 constant. Because the radial motion of the particles is virtually the same for the same value of \mathcal{E}_0/V_0 (if the parameter ϵ is small compared to 1), the plot isolates the dependence of the azimuthal motion on electric field and velocity. From the figure we can see that for lower \mathcal{E}_0 and V_0 one has a larger local-time displacement in the proton vs. electron injections. This is an expected result as while for a constant \mathcal{E}_0/V_0 ratio the radial transport stays the same, the time it takes for a particle to be injected (i.e. the time it stays in the pulse) is longer for a lower velocity. The azimuthal drift in the background \mathbf{B} -field is independent of pulse velocity, so the longer the particle stays in the pulse the larger its net azimuthal excursion.

We note however that the actual maximum displacement will be the lesser of the theoretically-calculated one and the azimuthal width of the pulse (which as discussed is typically about 60°). If the azimuthal width of the pulse is significantly smaller than the calculated maximum displacement there will be no type-I particles and the total strength of the injection will significantly decrease.

In order to model the observed electron-proton displacement particles must not stay too long in the pulse. This can be accomplished by not allowing the pulse velocity to be too low, as well as by making the pulse “sharper”, i.e. decreasing its radial widths Δ_1 , Δ_2 and Δ_3 (which would also decrease the time spent in the pulse). Obviously, to maintain the same radial transport for a sharper pulse we will need to increase the ratio \mathcal{E}_0/V_0 . Figure 10 shows the azimuthal displacement for such a choice, with Δ values reduced in half: $\Delta_1 = \Delta_2 = \Delta_3 = 0.5 R_E$, but the ratio \mathcal{E}_0/V_0 doubled. For this case, we see that the azimuthal displace-

ment is significantly reduced, but it still reaches large values for very low velocity and electric field.

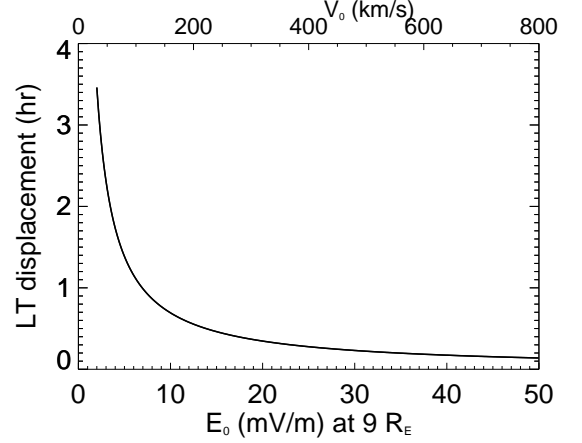


Figure 10. Similar to Figure 9, but for a pulse with half radial width and double \mathcal{E}_0/V_0 .

There is an important conclusion to be derived from our discussion here, which is that the pulse cannot have too low a velocity, as then the displacement between the proton and electron injection regions would be very large (if the pulse is wide enough), a fact not supported by observations. If the pulse is very narrow in local time on the other hand, such a combination would result in very little energization. This limitation on the pulse velocity and width is an additional constraint imposed by observations onto our model parameters \mathcal{E}_0 , V_0 , Δ and $\delta\phi$. However, the severity of the constraint is mitigated by the fact that we have only considered type-I particles. Therefore, the fact that we obtain a (slightly) larger displacement than the observed average does not mean that our pulse velocity (and electric field) are too low, but rather that there are other particles making contributions to an actual injection besides the type-I particles. The velocity limitation is also not so stringent if we allow for a narrower pulse in radial extent, coupled with larger pulse electric fields. Having a too narrow pulse, however, could be precluded by the possible dispersion of the pulse as it approaches Earth, but the treatment of such dispersion is beyond the scope of the present work.

4. Application — Computation of Injected Electron Fluxes in a Substorm Event

In this section we will model an actual substorm injection event, by computing the injected particle fluxes at the locations of several satellites registering the event and comparing them with actual satellite observations. In order to allow a comparison with our previous model results [Zaharia *et al.*, 2000] we will study the same substorm electron injection as analyzed before, the event on January 10, 1997 starting at around 4:30 universal time (UT).

4.1. Flux computation

As before, we use our analytical orbit solutions to compute the electron flux for this event, keeping in mind that our solutions for the particle motion, while non-relativistic, are suitable for application to electrons of “substorm energies” (less than 400 keV).

There are two ways of finding the injected flux, and both make use of Liouville’s phase space density conservation theorem. The first method is tracing particles backwards in

time [Birn *et al.*, 1997b] from the final location to their initial position. With such an approach, realizing that at a certain position and moment in time one might have particles with different initial locations that entered different parts of the pulse, one needs to perform an “averaging” procedure over a certain phase space neighborhood [Birn *et al.*, 1997b]. The other way of obtaining the flux is, instead of tracing particles back in time, to consider a “seed” particle population and follow their motion in the pulse by integrating the equations of motion either numerically [Li *et al.*, 1998] or analytically [Zaharia *et al.*, 2000]. Thus, at any location where the flux is needed, it can be computed based on the proportion of particles arriving in the vicinity of that location, as well as their initial energies and positions, using Equation (22). As in our previous work, we will employ here this latter method for computing the injected flux.

Once the differential flux is found at the injection location for each energy, we integrate the flux over an energy range of interest. As before, we distribute the seed particles every 1000 km between $6 R_E$ and $9 R_E$, every 1° in azimuth

and having 40 different energy channels within each energy range of interest (the values of the last two parameters will lead to a higher density of test particles than in the previous study however). The particle cells thus constructed are spaced densely enough so that the motion of phase space points from the same cell is not chaotic, i.e. a slight variation in initial location and energy does not influence the final values much [Birn *et al.*, 1997b]. We usually run the flux computation code with a time step of 100 s. The number loss of energetic particles after injection (presumably due to precipitation caused by pitch-angle scattering) is modeled as well, through multiplication with an exponentially decaying function in time, with an e -folding time for electrons of 3 hours for our energy ranges, as before.

4.2. Comparison of model results

The pulse parameters we initially choose for the event are similar to the ones considered before: $\mathcal{E}_0 = 4.5 \text{ mV/m} \cdot 9 R_E$, $V_0 = 125 \text{ km/s}$, $\Delta_1 = \Delta_2 = \Delta_3 = 11,000 \text{ km}$, and $2\delta\phi = 40^\circ$. The pulse has no azimuthal “offset”, i.e. is taken as

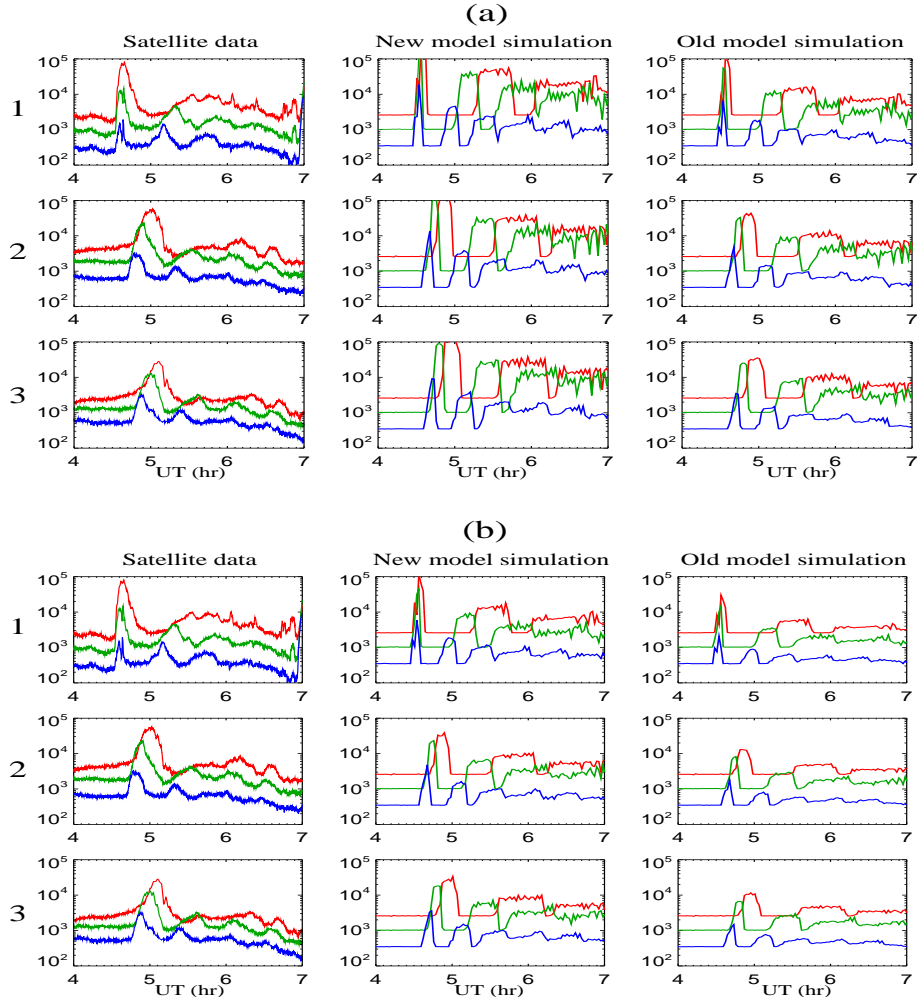


Figure 11. (a) Energetic electron differential fluxes ($\text{cm}^{-2}\text{s}^{-1}\text{sr}^{-1}\text{keV}^{-1}$) vs. universal time on Jan. 10, 1997, for three energy ranges at $6.6 R_E$, as measured by three LANL satellites (left column) and also as computed at each satellite position using the old model [Zaharia *et al.*, 2000] (right column) and the new model with stretched background (center column), with pulse electric field value of 4.5 mV/m at $9 R_E$. (b) Comparison of the same observed fluxes (left column) with computed fluxes using the new model (center column) and the old model (right column), but this time with a lower electric field of 3.5 mV/m at $9 R_E$. The numbers 1, 2 and 3 on the left-hand side refer to the three satellites: 1 is close to midnight (LANL satellite 1990-095, at LT = UT - 2:30), while 2 and 3 are further east on the dayside (2 represents satellite 1991-080, at LT = UT + 4:42, while 3 is LANL satellite 1994-084, at LT = UT + 6:54).

before to be centered around midnight. The dipole magnetic field parameter is chosen as $B_E = 0.3$ G, while the electron distribution parameters are taken to be $\kappa = 4$ and $\varepsilon = 2$ keV. This value for ε is consistent with reports that the average electron energy in the 6 to $9 R_E$ region during the late growth phase can be as large as a few keVs [Lui, 1996; Cheng and Lui, 1998]. The farthest initial radial distance R_i of electrons that can be dragged by the pulse to geostationary orbit is found to be $8.3 R_E$, compared to $8.5 R_E$ using the previous model (with the above parameters). These electrons transported over the largest radial distance (i.e. of type I) are also those that will experience the largest energy increase: the ratio of final vs. initial energy for the above parameters is 2.45 times in the current model vs. only 1.98 using a dipolar background.

Let us discuss a few features of the modeled injection event. If we start our time origin ($t = 0$) at the time when the front edge of the pulse arrives at $8.3 R_E$, the pulse will reach geosynchronous orbit at $t \approx 1$ min 30 s. Shortly afterwards the first electrons to make up the injection will arrive, from initial distances very close to $6.6 R_E$, however their flux increase will be modest. On the other hand, the electrons contributing most to the flux increase will be those of type I, which will arrive from $8.3 R_E$ at geosynchronous orbit in the tail of the pulse at time $t_3 \approx 4$ min. Therefore the initial injection peak at geosynchronous orbit in the azimuthal center of the pulse will span a time interval of about 2 min 30 s. During this short time interval, particles with a wide energy range will be swept to geostationary orbit in the vicinity of midnight local time, accounting for the “dispersionless” nature of the injection there. For observation points (satellites) away from the initial injection region, there will be a dispersed signature in the particle flux, with high-energy particles being registered earlier than lower-energy ones, due to their faster grad B drift from the injection location to the satellite.

The values for the pulse parameters chosen for this event were found after trying different sets of parameters in order to obtain good agreement between the observed injected flux and the flux computed using the *old model*, as seen in Figure 11(a). The left column of the figure shows the electron fluxes for three energy ranges as registered by three geosynchronous Los Alamos National Laboratory (LANL) satellites. The first satellite, 1990-095, is at about 2:00 local time (LT) during this event, and sees a dispersionless injection. Satellites 1991-080 and 1994-084 are eastward of the first one, at 10:00 and 12:00 LT, respectively, and register dispersion due to the different azimuthal drifts for different electron energies.

The right column in Figure 11(a) shows the computed fluxes using the old model with the chosen parameters. As with the similar parameters used before [Zaharia et al., 2000], one sees that the old model does a very good job of predicting the essential features of the electron injection at all 3 satellites: injected flux/background levels, dispersionless signature at the satellite near midnight (1990-095), shape of injected fluxes. The small-scale fluctuations observed in later drift echoes in the simulation are due to the finite number of cells considered and the time step used for plotting. There are also differences between theory and observation (such as simulated peaks being sharper than observed ones), mainly because the model only takes into account 90° pitch-angle particles, while the satellite sensors register all particles.

Finally, the center column of Figure 11(a) shows the computed fluxes using the new model (with stretched background field before the pulse), but still with the same parameters. While all particles in the new model arrive from closer to Earth than in the old model ($8.3 R_E$ vs. $8.5 R_E$), one can see that the modeled injected flux peaks are still larger than observed. This strengthens our earlier conclusion, obtained

for type-I particles only, that while the transport is lower, the energization is higher in the present model. In order to obtain congruence with observations using the new model, we need to decrease the strength of the injection by adjusting the pulse parameters in one or more of the following ways: decreasing \mathcal{E}_0 , increasing V_0 , or decreasing the radial width of the pulse. We choose to modify the electric field, and we find good agreement with observations in the injected electron fluxes computed by using the *new model* this time for the value $\mathcal{E}_0 = 3.5$ mV/m $\cdot 9 R_E$, as shown in Figure 11(b). There, the center column again shows the fluxes obtained with the new model, but this time with the lower **E**-field. We note that with the decreased **E**-field the initial particle location also decreases, to less than or equal to $7.8 R_E$. To show that the old model with the lower **E**-field cannot reproduce the observed injected flux levels, we plot in the right column of Figure 11(b) fluxes computed with the old model with a dipolar background and with the lower electric field, fluxes which are seen to be significantly lower than the observed ones.

This quantitative study of electron fluxes during an actual injection event modeled with both the old and the new models strengthens our conclusion reached before, that with the more realistic background magnetic field (stretched before the pulse) the particle energization is much stronger than with a dipole background. Thus, the model represents an even more effective mechanism for energizing particles during substorms, and the particles injected at geostationary orbit mainly arrive from the close vicinity of that orbit (1 to $2 R_E$ away).

5. Summary and Discussion

Extending previous work [Zaharia et al., 2000], we have investigated substorm injections by considering particle interaction with an Earthward-propagating electromagnetic pulse superposed over a non-dipolar, time-dependent background magnetic field. The particles are swept Earthward by the pulse via $\mathbf{E} \times \mathbf{B}$ drift to regions of higher B-field while conserving their magnetic moment, thus experiencing large energy increase through the betatron acceleration mechanism.

In contrast to test particle calculations in time-varying MHD fields [Birn et al., 1997b, 1998], the present approach does not model the field dynamics self-consistently. However, our approach captures the major acceleration mechanism identified in the investigations of Birn et al., namely the spatial localization and earthward propagation of the induced cross-tail electric field, and it permits a much easier study of the influence of the characteristics of the electric field pulse on the particle acceleration. Our approach also bypasses the initiation mechanism that causes the formation and propagation of the electromagnetic pulse. It therefore does not discriminate between alternative models of substorm initiation [e.g., Baker et al., 1996; Lui and Murphree, 1998].

The major difference of the current work from our previous study [Zaharia et al., 2000] is the assumption that the background magnetic field changes from a stretched tail-like field to a dipolar configuration, whereas the previous background field was dipolar before and after the passage of the pulse. The present field thus more closely resembles the changes from the substorm growth phase to the subsequent relaxation to a more dipolar field. As in the previous study, we have obtained entirely analytical solutions for the particle gyrocenter motion in the combined pulse and background fields, by choosing a three-part trapezoidal shape for the pulse amplitude dependence in the radial direction and considering the pulse to exist only in a limited local time extent (related to the substorm current “wedge”).

Our model is general in the sense that any radial wave form can be approximated by trapezoidal segments, with subsequent solutions for the motion and particle fluxes easily computed. Once analytical solutions are found for the motion, computing the injected particle fluxes using Liouville's theorem is straightforward and much less computer-intensive than a numerical integration of particle orbits. The computed fluxes reproduce very well geosynchronous satellite observations. Besides being able to model observed flux variations, our approach, through analytical solutions and a limited number of free parameters, also allows easy investigation of the effects of observational constraints (e.g. azimuthal injection displacement between protons and electrons) on parameter values. The model also provides an explanation for the observed “cutoffs” in injected fluxes during substorms, seen both at low and high energies.

As in our previous study, we found that the particles adiabatically injected to geostationary orbit have initial locations at less than $10 R_E$ from Earth. While this conclusion is different from the one obtained by *Li et al.* [1998], a later study by *Sarris et al.* [2002], using a refined version of the model of *Li et al.*, with a pulse narrower in local time, reached a similar conclusion (see Figure 10 of [*Sarris et al.*, 2002]).

The key word in the paragraph above is “adiabatically.” While proton and electron motion are adiabatic indeed for distances closer than $12 R_E$ as we have shown, protons might lose adiabaticity for farther distances in the stretched tail **B**-field. It could be possible for some protons to arrive from larger distances, however non-adiabatically, and only to move adiabatically in the last part of their trajectory, which we follow with our model. In such a scenario, however, most of the energization is still likely to occur during the adiabatic motion in the near-Earth region, as simulations [*Birn et al.*, 2003] considering both adiabatic and non-adiabatic motion suggest.

Another scenario in which particles arrive adiabatically from larger distances would occur if the contours of constant B in the equatorial plane connected the injection location near midnight to regions farther away in the tail at other local times. For 90 degree pitch-angle particles, the constant B contours are also drift contours (if convection is neglected) in the background field [*Zaharia and Cheng*, 2003b]. While such “concave” contours probably do not extend to geosynchronous during quiet times (for such contours in the T96 model, see for example Figure 3 of [*Zaharia and Cheng*, 2003b]), this could be possible for the highly non-axisymmetric magnetic field established during the substorm growth phase.

The results from the current model vs. the previous one show that, while the radial transport is only slightly lower than previously found, the energization that particles undergo is greatly enhanced in the current case, due to the much larger ratio between the magnetic field at the final vs. initial particle location (i.e. due to the fact that the real field decreases faster with distance than the dipolar field in the vicinity of geostationary orbit). Recalling that in this work we have only “conservatively” modeled the field stretching during the growth phase, we expect higher stretching to lead to even higher energization and particle source closer to Earth. A related conclusion we draw from the study is that relatively modest dipolarization electric fields are sufficient for leading to the large observed increases in particle fluxes observed during substorms. The lower magnitude of the electric field needed in the new model compared to the previous study is more realistic for a typical substorm, therefore we can state that the new model provides a better fit to observations of substorm injections and better explains the ubiquity of the injections as one of the most reliable predictors of substorm onset.

It is noteworthy to mention that while in a typical substorm the pulse fields would not be large enough to provide

MeV-range energization, a recent study [*Ingraham et al.*, 2001] has shown that for a powerful magnetic storm accompanied by many substorms during its duration the betatron acceleration mechanism could explain not only the energization of the usual (100s keV-range) electrons, but also of relativistic electrons (up to several MeVs) observed at geostationary orbit. Dipolarization during such events would have to occur in a region significantly wider in azimuth than the typical substorm current wedge, due to the azimuthal cutoff mechanism. An alternate way for high-energy particles to be energized in a narrow pulse would however be multiple encounters with the pulse as they drift around the Earth (this would require a huge drift speed and thus is not possible for hundred keV-range particles). In what percentage of disturbed events betatron acceleration can lead to MeV-range energization is, however, still a question that needs to be answered by future studies.

In the end, we note that while the present model is improved with respect to the previous one that considered a dipolar background field, there are still aspects of the model that could undergo refinement in the future. Perhaps one of the remaining simplifications in most pressing need of being relaxed is the consideration of 90° pitch-angle particles only. Test particle simulations in time-varying MHD fields [*Birn et al.*, 1997b, 2003] have shown that these particles are energized the most; therefore, by only considering them one could over-predict the injected flux. Other features of the substorm injection could also be affected by neglecting other pitch angles: for example, there are indications [e.g., *Anderson and Takahashi*, 2000] from dayside observations that particles with pitch angles other than 90° arrive earlier at an observing satellite. While these effects would provide a “smoother” flux, we do not expect them to have a large effect on the peak flux values or other key injection features. They could however be a welcome addition in complexity to our model and smoothen the transition of the model goal from physical understanding to predictive capabilities necessary for space weather forecast.

Appendix: Analytical Solutions for the Particle Motion

In this Appendix we present fully-analytical solutions of the drift equations (15) and (16) in the combined pulse and background fields, for each of the three parts of the trapezoidal dipolarization pulse.

Motion in the first part of the pulse

In the first part of the trapezoidal pulse we have $\mathcal{R} = (\xi - \xi_1)/\Delta_1$ (for more details and plots of particles entering/exiting each part of the pulse we refer the reader to our earlier work [*Zaharia et al.*, 2000]). Let us consider a particle at $t = t_i$ at initial position ($R_i = R_0 + \Delta$, ϕ_i) (where $0 \leq \Delta \leq \Delta_1$), R_0 is the radial location of the beginning of the pulse at t_i and $\phi_0 - \delta\phi \leq |\phi_i| \leq \phi_0 + \delta\phi$ in the fields of the pulse. If the particle enters the pulse radially one has $\Delta = 0$, otherwise Δ will have a non-zero value. The radial solution can be simply obtained from Equation (18):

$$\frac{2V_0 B_E R_E^3}{\mathcal{E}_0 \Delta_1} \left(\frac{1}{R} - \frac{1}{R_i} \right) + \left(\frac{\Delta}{\Delta_1} \right)^2 = \left[\frac{R - R_0 + V_0 (t - t_i)}{\Delta_1} \right]^2 - \frac{2\epsilon}{\Delta_1} [R - R_i + V_0 (t - t_i)] \quad (\text{A1})$$

The expression above is very similar to the formula found by *Zaharia et al.* [2000] for the case of a dipolar background, except for the second term (negative) on the right-hand side

(leading to apparently lower radial transport). The solution above is handy if one knows ξ , e.g. knows that the particle has exited a certain part of the pulse and wants to find its actual physical location. However, since in general $\xi = R + V_0 t$ is not known, the expression will have to be inverted to obtain a form $t = t(R)$.

For the azimuthal motion, as before, instead of trying to find $\phi(t)$, it is easier to solve for $\phi(R)$. From the ratio of $\mathbf{E} \times \mathbf{B}$ and ∇B -drifts, we easily find for the motion in the first and second parts of the pulse:

$$\frac{d\phi}{dR} = \frac{\mu}{q\mathcal{E}_0} \left(\frac{3B_E R_E^3}{\mathcal{R} R^4} - \frac{B_c}{\mathcal{R} R^2} + \frac{\mathcal{E}_0}{V_0 R^2} - \frac{\mathcal{E}_0}{V_0 R \mathcal{R}} \frac{\partial \mathcal{R}}{\partial R} \right) \quad (\text{A2})$$

The solution of the above equation for our particular form of \mathcal{R} can also be obtained analytically, in a form very similar to the one in our previous study:

$$\begin{aligned} \phi - \phi_i = & -\frac{6\mu}{q} \left(\frac{B_E R_E^3 \Delta_1}{2V_0 \mathcal{E}_0} \right)^{1/2} \left\{ \frac{1}{5} \left[\left(\frac{1}{R} - \frac{1}{a} \right)^{5/2} - \left(\frac{1}{R_i} - \frac{1}{a} \right)^{5/2} \right] + \frac{2}{3a} \left[\left(\frac{1}{R} - \frac{1}{a} \right)^{3/2} - \left(\frac{1}{R_i} - \frac{1}{a} \right)^{3/2} \right] + \right. \\ & \left. \frac{1}{a^2} \left[\left(\frac{1}{R} - \frac{1}{a} \right)^{1/2} - \left(\frac{1}{R_i} - \frac{1}{a} \right)^{1/2} \right] \right\} + \\ & \frac{\mu}{qV_0} \left\{ \left(\frac{1}{R_i} - \frac{1}{R} \right) + \left(\frac{\mathcal{E}_0 R_0}{2V_0^3 B_E R_E^3 \Delta_1} \right)^{1/2} \left[\sin^{-1} \left(\frac{2R_i}{a} - 1 \right) - \sin^{-1} \left(\frac{2R}{a} - 1 \right) \right] \right\}, \quad (\text{A3}) \end{aligned}$$

where $1/a = 1/R_i - [(\delta_1 + \epsilon)/G_1]^2$ and $G_1^2 = 2V_0 B_E R_E^3 / (\mathcal{E}_0 \Delta_1)$ are notations similar to the ones in our previous work. In addition, here we also made the notations $\delta_1 = \Delta/\Delta_1$ and $\epsilon = V_0 B_c / \mathcal{E}_0$. Equation (A3) reveals that the only difference from the formula obtained before [Equation (15) of [Zaharia et al., 2000]] is the lower value of $1/a$, which will decrease the extent of azimuthal motion compared to the previous case of a dipolar background.

Now let us analyze the conditions for a particle entering and exiting the first part of the trapezoidal pulse. If a particle has its local time within the azimuthal “wedge” of the pulse when the pulse arrives at its location then it will enter the pulse radially. If a particle enters the pulse azimuthally, then $\phi_i = \phi_0 + \delta\phi$ for protons and $\phi_i = \phi_0 - \delta\phi$ for electrons. Particles can exit this part (and therefore the whole pulse) azimuthally (if for example for a proton ϕ as given by Equation (A3) is less than $\phi_0 - \delta\phi$). Alternatively, a particle exits this part radially (and enters the second part of the pulse thereafter) at a position easily obtainable from Equation (A1), with $\xi = \xi_1$.

An important point to mention here is an effect which can allow a particle to stay longer in the pulse. Specifically, a particle is able to reverse its azimuthal motion in this part of the pulse (see Figures 5 and 10 of [Zaharia et al., 2000]) if the gradient of the pulse magnetic field is larger in magnitude than the gradient of the background field [Li et al., 1998; Zaharia et al., 2000], and thus could remain in the pulse without exiting it azimuthally for certain combinations of pulse parameters. For a proton, the eastward drift term responsible for the reversal effect is the last term in Equation (A3).

Motion in the second part of the pulse

We now analyze the motion of a particle entering the second part of the pulse at time t_i and position (R_i, ϕ_i) , at a dis-

tance Δ from the end of the second part ($R_i = R_1 + \Delta_2 - \Delta$, $0 \leq \Delta \leq \Delta_2$). Obviously, $\Delta \neq \Delta_2$ only for azimuthally-entering particles, and $\Delta = \Delta_2$ if the particle enters this part radially (coming from the first part of the pulse). Since $\mathcal{R} = 1$ in this part of the pulse, the radial solution can be obtained from Equation (19) in the simple form

$$\frac{1}{R} - \frac{1}{R_i} = \frac{\mathcal{E}_0 - V_0 B_c}{B_E R_E^3} [R - R_i + V_0(t - t_i)] \quad (\text{A4})$$

Comparing the expression above with the corresponding one for the case of a dipole field (Equation (27) in [Zaharia et al., 2000]), one again notices that the radial transport seems to be less effective in the current case (due to the lower electric field). The azimuthal solution can also be easily obtained by putting $\mathcal{R} = 1$ in Equation (A2), and is given by

$$\phi - \phi_i = \frac{\mu}{q} \left[\frac{B_E R_E^3}{\mathcal{E}_0 - V_0 B_c} \left(\frac{1}{R_i^3} - \frac{1}{R^3} \right) + \frac{1}{V_0} \left(\frac{1}{R_i} - \frac{1}{R} \right) \right] \quad (\text{A5})$$

again very similar to the formula obtained before, with the only difference being $\mathcal{E}_0 - V_0 B_c$ replacing \mathcal{E}_0 .

Motion in the third part of the pulse

Finally, we analyze the particle motion in the third part of our trapezoidal pulse, which is characterized by decreasing “pulse” fields, superposed on an increasing background \mathbf{B} -field that becomes dipolar at the end of the pulse. Let us follow a particle entering this part at time t_i and position (R_i, ϕ_i) , where $R_i = R_2 + \Delta_3 - \Delta$ ($0 \leq \Delta \leq \Delta_3$) and $|\phi_i| \leq \phi_0 + \delta\phi$. For this particle, the radial solution can be obtained from Equation (21) with the corresponding value for \mathcal{R} :

$$\frac{1}{R} - \frac{1}{R_i} = \frac{(\mathcal{E}_0 - V_0 B_c) \Delta_3}{2V_0 B_E R_E^3} \left\{ \frac{2[R - R_i + V_0(t - t_i)]}{\Delta_3} + \left(\frac{\Delta_3 - \Delta}{\Delta_3} \right)^2 - \left[\frac{R - R_2 + V_0(t - t_i)}{\Delta_3} \right]^2 \right\}, \quad (\text{A6})$$

which again can be viewed as a solution of the form $t = t(R)$. Particles entering this part radially ($\Delta = \Delta_3$) will experience the largest radial transport. Now regarding the azimuthal motion, Equation (A2) is not valid for motion in the third part of the pulse, and instead we have

$$\frac{d\phi}{dR} = \frac{\mu}{q(\mathcal{E}_0 - V_0 B_c)} \left(\frac{3B_E R_E^3}{\mathcal{R} R^4} + \frac{\mathcal{E}_0 - V_0 B_c}{V_0 R^2} - \frac{\mathcal{E}_0 - V_0 B_c}{V_0 R \mathcal{R}} \frac{\partial \mathcal{R}}{\partial R} \right), \quad (\text{A7})$$

which is again very similar to the equation for the case with dipole background [Equation (13) of [Zaharia et al., 2000]], but with $\mathcal{E}_0 - V_0 B_c$ replacing \mathcal{E}_0 . This is due to the fact that the total field configuration in the third part of the pulse consists in the “pulse” field superposed over the time-changing “background” field, a situation which can be summed as an “effective” pulse of amplitude $\mathcal{E}_0 - V_0 B_c$ superposed over a time-independent dipolar \mathbf{B} -field, of the kind analyzed in our previous work. We expect therefore the azimuthal solution to be very similar to the one obtained before, and indeed it is given by

$$\phi - \phi_i = \frac{6\mu}{q} \left[\frac{B_E R_E^3 \Delta_3}{2V_0 (\mathcal{E}_0 - V_0 \mathcal{B}_c)} \right]^{1/2} \left\{ \frac{1}{5} \left[\left(\frac{1}{b} - \frac{1}{R} \right)^{5/2} - \left(\frac{1}{b} - \frac{1}{R_i} \right)^{5/2} \right] - \frac{2}{3b} \left[\left(\frac{1}{b} - \frac{1}{R} \right)^{3/2} - \left(\frac{1}{b} - \frac{1}{R_i} \right)^{3/2} \right] + \frac{1}{b^2} \left[\left(\frac{1}{b} - \frac{1}{R} \right)^{1/2} - \left(\frac{1}{b} - \frac{1}{R_i} \right)^{1/2} \right] \right\} + \frac{\mu}{qV_0} \left(\frac{1}{R_i} - \frac{1}{R} \right) + \frac{\mu\sqrt{b}}{qV_0 G_3 \Delta_3} \ln \frac{2R - b + \sqrt{(2R - b)^2 - b^2}}{2R_i - b + \sqrt{(2R_i - b)^2 - b^2}}, \quad (\text{A8})$$

where $G_3^2 = 2V_0 B_E R_E^3 / [(\mathcal{E}_0 - V_0 \mathcal{B}_c) \Delta_3]$, $1/b = 1/R_i + (\delta_3/G_3)^2$ and $\delta_3 = \Delta/\Delta_3$. From the above expression one can see that in the third part of the pulse the background and pulse field gradients give rise to drifts in the same azimuthal direction, and so the (westward for protons, eastward for electrons) drift is more pronounced than in the second part.

Acknowledgments. This work was performed under the auspices of the U.S. Department of Energy, with LANL support for S. Zaharia in the form of an LDRD Director's Fellowship. Additional support is acknowledged from the U.S. Department of Energy's Office of Basic Energy Sciences through its Geosciences Research Program, the NASA's Sun Earth Connection Theory Program and the National Science Foundation through grant ATM-0202306.

References

- Aggson, T. L., J. P. Heppner, and N. C. Maynard, Observations of large magnetospheric electric fields during the onset phase of a substorm, *J. Geophys. Res.*, **88**, 3981, 1983.
- Anderson, B. J., and K. Takahashi, Pitch angle dispersion of ion injections, *J. Geophys. Res.*, **105**(A8), 18,709, 2000.
- Baker, D. N., R. D. Belian, P. R. Higbie, and E. W. Hones, High-energy magnetospheric protons and their dependence on geomagnetic and interplanetary conditions, *J. Geophys. Res.*, **84**, 7138, 1979.
- Baker, D. N., T. I. Pulkkinen, V. Angelopoulos, W. Baumjohann, and R. L. McPherron, Neutral line model of substorms: Past results and present view, *J. Geophys. Res.*, **101**, 12,975, 1996.
- Behlke, A., I. Tsagouri, and H. Mavromichalaki, Study of the longitudinal expansion velocity of the substorm current wedge, *Ann. Geophys.*, **16**, 1423, 1998.
- Belian, R. D., D. N. Baker, P. R. Higbie, and E. W. Hones, High-resolution energetic particle measurements at 6.6 R_E , 2. high-energy proton drift echoes, *J. Geophys. Res.*, **83**, 4857, 1978.
- Birn, J., M. F. Thomsen, J. E. Borovsky, G. D. Reeves, D. J. McComas, and R. Belian, Characteristic plasma properties during dispersionless substorm injections at geosynchronous orbit, *J. Geophys. Res.*, **102**(A2), 2309, 1997a.
- Birn, J., M. F. Thomsen, J. E. Borovsky, G. D. Reeves, D. J. McComas, R. D. Belian, and M. Hesse, Substorm ion injections: Geosynchronous observations and test particle orbits in three-dimensional dynamic MHD fields, *J. Geophys. Res.*, **102**, 2325, 1997b.
- Birn, J., M. F. Thomsen, J. E. Borovsky, G. D. Reeves, D. J. McComas, R. D. Belian, and M. Hesse, Substorm electron injections: Geosynchronous observations and test particle simulations, *J. Geophys. Res.*, **103**(A5), 9235, 1998.
- Birn, J., M. F. Thomsen, and M. Hesse, Electron acceleration in the dynamic magnetotail, submitted to *Phys. Plasmas*, 2003.
- Cheng, C. Z., and A. T. Y. Lui, Kinetic ballooning instability for substorm onset and current disruption observed by AMPTE/CCE, *Geophys. Res. Lett.*, **25**, 4091, 1998.
- Christon, S. P., D. J. Williams, D. G. Mitchell, C. Y. Huang, and L. A. Frank, Spectral characteristics of plasma sheet ion and electron populations during disturbed geomagnetic conditions, *J. Geophys. Res.*, **96**, 1, 1991.
- Clauer, C. R., and R. L. McPherron, Mapping the local time-universal time development of magnetospheric substorms using mid-latitude magnetic observations, *J. Geophys. Res.*, **79**(19), 2811, 1974.
- Delcourt, D. C., Particle acceleration by inductive electric fields in the inner magnetosphere, *J. Atmos. Solar-Terr. Phys.*, **64**, 551, 2002.
- Delcourt, D. C., J. A. Sauvaud, and A. Pedersen, Dynamics of single-particle orbits during substorm expansion phase, *J. Geophys. Res.*, **95**(A12), 20,853, 1990.
- Erickson, G. M., N. C. Maynard, W. J. Burke, J. R. Wilson, and M. A. Heinemann, Electromagnetics of substorm onsets in the near-geosynchronous plasma sheet, *J. Geophys. Res.*, **105**(A11), 25,265, 2000.
- Fairfield, D. H., et al., Geotail observations of substorm onset in the inner magnetotail, *J. Geophys. Res.*, **103**(A1), 103, 1998.
- Friedel, R. H. W., A. Korth, and G. Kremser, Substorm onsets observed by CRRES: Determination of energetic particle source regions, *J. Geophys. Res.*, **101**(A6), 13,307, 1996.
- Ingraham, J. C., T. E. Cayton, R. D. Belian, R. A. Christensen, R. H. W. Friedel, M. Meier, G. D. Reeves, and M. Tuszewski, Substorm injection of relativistic electrons to geosynchronous orbit during the great magnetic storm of March 24, 1991, *J. Geophys. Res.*, **106**(A11), 25,759, 2001.
- Kaufmann, R. L., Substorm currents: Growth phase and onset, *J. Geophys. Res.*, **92**(A7), 7471, 1987.
- Li, X., D. N. Baker, M. Temerin, G. D. Reeves, and R. D. Belian, Simulation of dispersionless injections and drift echoes of energetic electrons associated with substorms, *Geophys. Res. Lett.*, **25**, 3763, 1998.
- Liou, K., C.-I. Meng, A. T. Y. Lui, P. T. Newell, and S. Wing, Magnetic dipolarization with substorm expansion onset, *J. Geophys. Res.*, **107**(A7), doi:10.1029/2001JA000179, 2002.
- Lopez, R. E., D. G. Sibeck, R. W. McEntire, and S. M. Krimigis, The energetic ion substorm injection boundary, *J. Geophys. Res.*, **95**, 109, 1990.
- Lui, A. T. Y., Current disruption in the Earth's magnetosphere: Observations and models, *J. Geophys. Res.*, **101**, 13,067, 1996.
- Lui, A. T. Y., and J. S. Murphree, A substorm model with onset location tied to an auroral arc, *Geophys. Res. Lett.*, **25**, 1269, 1998.
- Maynard, N. C., W. J. Burke, E. M. Basinka, G. M. Erickson, W. J. Hughes, H. J. Singer, A. G. Yahnin, D. A. Hardy, and F. S. Mozer, Dynamics of the inner magnetosphere near times of substorm onsets, *J. Geophys. Res.*, **101**(A4), 7705, 1996.
- Moore, T. E., R. L. Arnoldy, J. Feynman, and D. A. Hardy, Propagating substorm injection fronts, *J. Geophys. Res.*, **86**, 6713, 1981.
- Reeves, G. D., New perspectives on substorm injections, in *Substorms-4, Proc. ICS-4*, edited by S. Kokubun and Y. Kamide, p. 785, 1998.
- Reeves, G. D., T. A. Fritz, T. E. Cayton, and R. D. Belian, Multi-satellite measurements of the substorm injection region, *Geophys. Res. Lett.*, **17**, 2015, 1990.
- Reeves, G. D., M. G. Henderson, P. S. McLachlan, and R. D. Belian, Radial propagation of substorm injections, in *Substorms 3*, edited by ESA, p. 579, ESA Publications Division, 1996.
- Roederer, J. G., *Dynamics of Geomagnetically Trapped Radiation*, 87 pp., Springer-Verlag, New York, 1970.
- Russell, C. T., and R. L. McPherron, The magnetotail and substorms, *Space Sci. Rev.*, **15**, 205, 1973.
- Sarris, T. E., X. Li, N. Tsaggas, and N. Paschalidis, Modeling energetic particle injections in dynamic pulse fields with varying propagation speeds, *J. Geophys. Res.*, **107**(A3), 1033, doi: 10.1029/2001JA900166, 2002.
- Schulz, M., and M. W. Chen, Bounce-averaged Hamiltonian for charged particles in an axisymmetric but nondipolar model magnetosphere, *J. Geophys. Res.*, **100**(A4), 5627, 1995.
- Shepherd, G. G., et al., Plasma and field signatures of poleward propagating auroral precipitation observed at the foot of the Geos 2 field line, *J. Geophys. Res.*, **85**, 4587, 1980.
- Thomsen, M. F., J. Birn, J. E. Borovsky, K. Morzinski, D. J. McComas, and G. D. Reeves, Two-satellite observations of substorm injections at geosynchronous orbit, *J. Geophys. Res.*, **106**(A5), 8405, 2001.
- Tsyganenko, N. A., Modeling the Earth's magnetospheric magnetic field confined within a realistic magnetopause, *J. Geophys. Res.*, **100**, 5599, 1995.

- Tsyganenko, N. A., and D. P. Stern, Modeling the global magnetic field of the large-scale Birkeland current systems, *J. Geophys. Res.*, *101*, 27,187, 1996.
- Vasyliunas, V. M., A survey of low-energy electrons in the evening sector of the magnetosphere with OGO 1 and OGO 3, *J. Geophys. Res.*, *73*, 2839, 1968.
- Zaharia, S., and C. Z. Cheng, Near-earth thin current sheets and Birkeland currents during substorm growth phase, *Geophys. Res. Lett.*, *30*(17), 1883, doi:10.1029/2003GL017456, 2003a.
- Zaharia, S., and C. Z. Cheng, Can an isotropic plasma pressure distribution be in force balance with the T96 model field?, *J. Geophys. Res.*, *108*(A11), 1412, doi:10.1029/2002JA009501, 2003b.
- Zaharia, S., C. Z. Cheng, and J. R. Johnson, Particle transport and energization associated with substorms, *J. Geophys. Res.*, *105*, 18,741, 2000.
-
- J. Birn, R. H. W. Friedel, G. D. Reeves, M. F. Thomsen, Sorin Zaharia, Los Alamos National Laboratory, P.O. Box 1663, MS D466, Los Alamos, NM 87545 (e-mail: szaharia@lanl.gov)
- C. Z. Cheng, Princeton Plasma Physics Laboratory, P.O. Box 451, Princeton, NJ 08543